A Phase field method for modeling stress corrosion crack propagation in a nickel base alloy

Thanh Tung T.T. Nguyen, José Bolivar, Julien Réthoré, Marie-Christine Baietto, Marion Fregonese

To cite this version:

Thanh Tung T.T. Nguyen, José Bolivar, Julien Réthoré, Marie-Christine Baietto, Marion Fregonese. A Phase field method for modeling stress corrosion crack propagation in a nickel base alloy. International Journal of Solids and Structures, 2017, 10.1016/j.ijsolstr.2017.02.019 . hal-01469321

A Phase field method for modeling stress corrosion crack propagation in a nickel base alloy

Thanh-Tung Nguyen[a], José Bolivar[b], Julien Réthoré[a], Marie-Christine Baietto[a], Marion Fregonese[b]

[a]*LaMCoS, Université de Lyon / INSA Lyon / CNRS UMR 5259*
27 Avenue Jean Capelle, F-69621 Villeurbanne, Cedex, France
[b]*MATEIS, Université de Lyon / INSA Lyon / CNRS UMR 5510*
21 Avenue Jean Capelle, F-69621 Villeurbanne, Cedex, France

Abstract

Stress Corrosion Cracking (SCC) is a very common failure mechanism characterized by a slow, environmentally influenced crack propagation in structural components. The mechanisms proposed to explain, at the microscopic scale, the cracking propagation processes are not able to elucidate all aspects of this phenomenon in different metal/environment systems. This work is concerned with the development of a new multiphysics model for understanding the phenomena of crack propagation under the effect of SCC. This new model is based upon: (i) a Phase field method, based on a variational formulation of brittle fracture with regularized approximation of discontinuities; (ii) a robust algorithm capable to prescribe the displacements (over the boundary of a small sub-volume) and crack onset obtained by image processing based on digital image correlation in the sample during the numerical simulations; (iii) a coupling with a diffusion model informed with first-principles

---

Email address: `julien.rethore@ec-nantes.fr` (Julien Réthoré)

[1] Now at GEM, CNRS UMR 6183 CNRS / Ecole Centrale de Nantes / Université de Nantes

computations of diffusion coefficient. In this new model, the phenomenon of environmentally assisted cracking phenomena was successfully represented as well the interactions between cracks and the subsequent shielding effects. The analyses, performed on several samples of Inconel 600 alloy containing a crack network, show a remarkable agreement between the crack morphology and history obtained by the model and by the experiments.

Keywords: Stress Corrosion Cracking, Crack propagation, Phase field, Digital Image Correlation, Slip dissolution, Crack coalescence, Complex crack networks

1. Introduction

Predicting the strength and durability of engineering components and structures using numerical simulations of fracture phenomena induced by Stress Corrosion Cracking (SCC) is a very challenging problem. SCC can often be regarded as the result of localized oxidation enhanced by stress/strain: a combined action of a sustained mechanical loading and a chemically aggressive environment. The occurrence of SCC in a structure can lead to catastrophic failures, it has thus long been recognized as potentially dangerous. One of the mechanisms responsible for this process noted in the literature is the embrittlement of the material due to local anodic dissolution of fresh metal created by slip band emergence at the crack tip. In this area recent developments and corresponding issues have been reviewed in Newman and Healey (2007), followed by some original contributions related to different aspects of the problem: loading rate effects, harmonization of different formulations of the model, and sensitivity of the model to various parameters. Developing numerical models for the quantitative evaluation of stress corrosion cracking growth rates in terms of key engineering parameters is highly required.

Various experimental methods have been proposed in the literature to study cracks induced by SCC. The measurements of corrosion contribution is usually based on electrochemical methods such as Electrochemical Noise (EN) Hladky and Dawson (1981); Kearns (1996); Kovac et al. (2010). Thanks to its capacity of distinguishing between different corrosion types, the (EN) method is mostly applied to detect and evaluate SCC activity. Acoustic Emission (AE) Bellenger et al. (2002); Jomdecha et al. (2007); Shaikh et al. (2007) is also widely used because of its ability to detect material deformation, cracking and fracture. Many microscopy techniques have been applied to characterize SCC at different scales. For example, magnetic force microscopy (MFM) has been used to detect the chromium depleted regions of type 304 stainless steel Takaya et al. (2004), the early stages of pitting and localized corrosion have been studied by combining *in situ* observations and electromechanical atomic force microscopy (EAFM) Williford et al. (2000), and scanning electron microscopy (SEM) is used to study the pitting corrosion of Al Richardson and Wood (1970). This technique is also used to observe the fracture surface of SCC in high strength steel fasteners Abhay et al. (2010). The Diffraction Contrast Tomography (DCT) is another technique used to characterize SCC, for example the work of King et al. (2008) study the interaction between intergranular stress corrosion cracking and microstructure in a Grain-Mapped Polycrystal. In the work of Babout et al.

(2006), the phenomenon of intergranular stress corrosion cracking in a sensitised type 302 stainless steel wire has been observed *in situ* using high resolution X-ray microtomography. An important step after image acquisition by OM/SEM is the processing of microstructural images to obtain a qualitative/quantitative analysis of the sample. Many techniques have been developed in the literature with this aim. Among these techniques, digital image correlation (DIC), or digital volume correlation (DVC) in 3D, is one of the most efficient and versatile tool. This procedure is based on the comparison of images acquired at different stages of a mechanical test and provides quantitative descriptions of local deformation. DIC could be used instead of, or in addition to the prevailing methods to detect defects, by observing the singularity due to the change in the strain distribution, or a step jump in the displacement field across the cracks.

In the literature, most of the models proposed to predict SCC rates are based on linear elastic fracture mechanics concepts without deeply considering corrosion kinetics. A numerical simulation scheme of SCC is developed in the work of Choi et al. (2007) for a thermoplastic material based on crack layer theory. SCC is here considered as a superposition of creep, it induces aging and chemical degradation. Then, they use the phenomenological power laws to describe the loss of material toughness due to these two mechanisms. In addition, this work proposed a generic kinetic parameter to represent the rate of chemical corrosion. Both SCC and mechanically driven crack growth were simulated. In the work of Saito and Kuniya (2001), a predictive methodology for SCC crack growth using a mechanochemical model based on a slip formation/dissolution mechanism is presented. The mechanochemical model consists of the combined kinetics of the plastic deformation process as a mechanical factor and the slip dissolution-repassivation process as an environmental factor at the crack tip. The role of the passive film has also been studied in many works, its physical degradation is usually expressed by a unique parameter namely the "crack tip strain rate". Many works in literature use this concept that is applied to study SCC in many cases, such as those by Vermilyea (1972); Vermilya and Diegle (1976), Parkins (1980, 1987), Ford and Andresen (1987),... However, the results of these models are rarely compared with experimental ones, especially concerning crack morphology.

With recent advances in numerical simulation methods new studies are now possible, allowing the development of fracture models at microscale, in particular for complex cracks morphology including phenomena of crack initiation, coalescence and propagation. The objective of this proposed paper is to construct a numerical model to simulate the failure of a nickel base alloy under SCC in an acidified tetrathionate environment. The reaction-dissolution process is simulated with a kinetics model, and integrated into a mechanical analysis. The anodic dissolution, that is involved in the decrease of fracture property is considered to be dependent on the extent of corrosion, and such dependence is implemented within a fracture model. For this purpose, we use the phase field method based on the variational formulation of the crack evolution problem due to Francfort and Marigo (1998). The regularized setting of their framework has been considered in Bourdin et al. (2000). Another contribution for the phase field method based on LandauGinzburg type phase-field evolution equations can be found in Karma et al. (2001). The phase field method may be approached both theoretically and practically, providing an excellent framework for taking into account environmental effects on the failure phenomenon. This framework is also extremely suitable for establishing parametric trends besides enabling the assessment of safety margins. This work is concerned with the development of a new multiphysics model for simulating the phenomena of crack propagation under the effect of SCC based on the phase field method and the numerical implementation proposed by Miehe et al. (2010). Direct comparisons between the simulationed crack paths and experimental data are performed. In addition, a strategy is proposed to identify the parameters of the constitutive model by using DIC results.

The overview of the paper is as follows. A brief introduction of experimental methods is described in section 2. Then, we present a short review about the slip dissolution model for SCC in section 3. The new model proposed for SCC propagation based on the phase field method is presented in section 4. The proposed algorithm is described in section 5. Finally, the method is evaluated and illustrated by damage benchmarks and practical examples involving crack onset and propagation provided by SCC, and then we present the direct comparisons between the model and the experiments in section 6.

2. Experimental method for observation of crack propagation

2.1. Experimental procedures

This study focuses on Inconel 600 alloy material. Its chemical composition is given in Table 1. The presented experiments were performed on specimens with a gauge dimension of 117 mm length, 8 mm width and 2 mm thickness as depicted in Fig. 1(a). (see Bolivar et al. (2016) for more details of sample preparation)

Elements	Ni	Fe	Cr	Mn	Cu	Co	Ti-Al	C	S
Wt. Pct.	bal.	9.25	15.52	0.12	0.1	0.1	0.25	0.03	0.002

Table 1: Composition of the Inconel 600 alloy

To use DIC, a specific procedure has been proposed to improve the grey level contrast on the sample surface. Finally, the samples exhibit many random heterogeneities that give local contrast of grey levels in the images, what is promising for DIC. The details of experimental setup has been described in Bolivar et al. (2016)

Constant load tests were performed for this study. First, the samples are immersed in the test solution (10 mM $K_2S_4O_6$, pH = 3) for about 45 minutes. Then, the specimens are subjected to a constant applied load corresponding to 80 % of the yield stress (263 MPa) by using an electromechanical tensile machine (LLOYD LR30K Plus).

The sample surface was observed in-situ through a 2/3” CCD Stingray

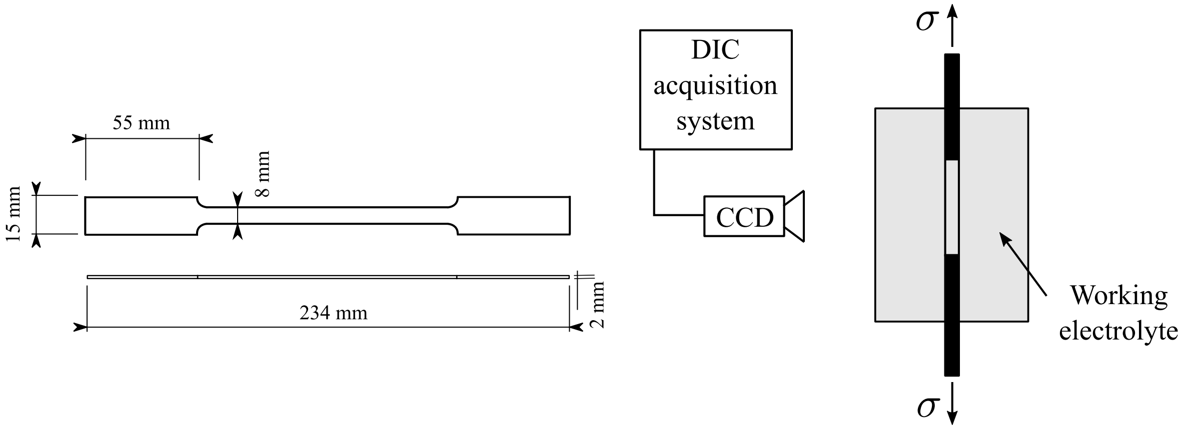

(a) (b)

Figure 1: Description of experimental procedures: (a) geometry of specimen and counter electrode (b) schematic illustration of experimental set-up

camera of 5 Mpx with a pixel size of 3,45 μm (see Fig. 1(b)). The camera was coupled with a 1X telecentric lens. The surface was enlighted with a led lamp in order to eliminate the light variation on the surface. Two polarizing filters (linear and circular) were also used in order to avoid light reflection.

The test is stopped when crack colonies are observed and the electric potential is stable (around -195 mv/SCE). Finally, we use either Optical Microscopy (OM) or Scanning Electron Microscopy (SEM) to observe the cracked surfaces, this step will be used to validate the results of crack detection by DIC.

2.2. Detection of crack network by using image processing based on DIC

DIC is a full-field measurement technique, based on the comparison of images acquired at different stages of a mechanical test. DIC provides access the displacement field at the surface of the sample. DIC principles have been introduced in experimental solid mechanics more than 20 years ago by Sutton et al. (1983) and this technique is currently used for many applications.

We refer to references Sutton et al. (2009) for a detailed description of this technique. The specific 2D-DIC procedure used in this work is similar to the one used in reference Besnard et al. (2006).

The DIC analysis is performed using the in-house software. The procedure is based on four main steps:

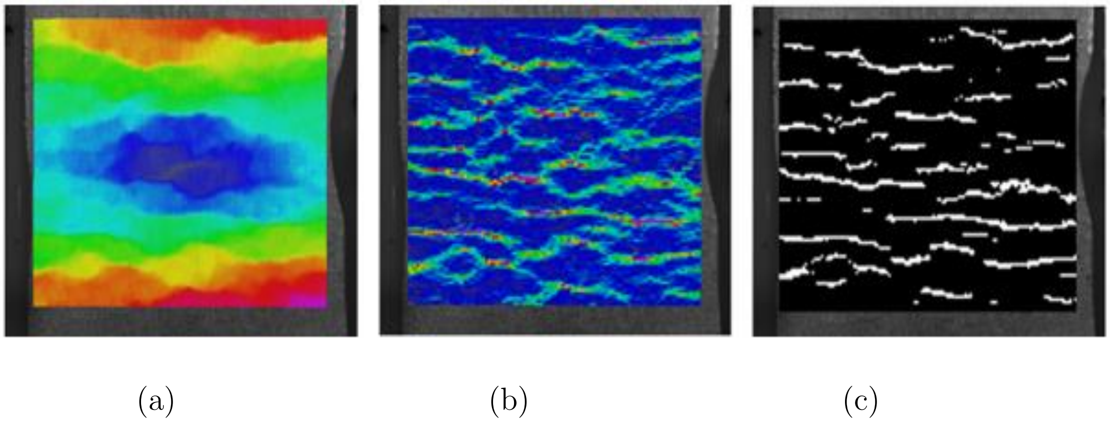

Figure 2: Crack detection by using image processing based on DIC: (a) displacement field; (b) Postprocessed displacement fields; (c) crack paths obtained by segmentation

- **DIC analysis:** the correlation analysis is performed. We use here a mesh size of 16 pixels (55 μm). After this step, we obtain the displacement fields for series of deformed images (see Fig. 2(a)).
- **Postprocessing displacement fields:** crack detection by using only displacement field is not straightforward see Fig. 2(a). A method has

been proposed to reduce the noise and increase the contrast due to displacement jumps. This method is based on the removal of Rigid Body Movement (RBM) and the displacement due to the overall homogeneous strain. A median filter is subsequently applied to the resulting displacement to remove the fluctuation that doesn't have a discontinuity feature. Then, the element-wise displacement variations in the loading direction are calculated. The obtained result is depicted in Fig. 2(b)

- **Crack extraction:** a segmentation procedure is performed to extract the cracked area from the post-processed displacement field. In this example, we perform the extraction of cracks by using the classical threshold criterion for the post-processed displacement field (threshold value 0.45 μm). The obtained result is depicted in Fig. 2(c).
- **Parameters identifications:** Finally, cracks are labeled and followed during the image sequence. We also identify several fracture parameters such as: crack length, crack growth rate, crack initiation...(see Bolivar et al. (2016) for more details)

In this work, DIC crack extraction results will be compared with those of the numerical simulation. For this purpose, an algorithm is proposed to construct input modeling from these data, this procedure will be introduced in Section 6.2.1.

3. Slip dissolution model for stress corrosion cracking

One of the models that successfully rationalizes the phenomenology and the kinetics of stress-corrosion cracking (SCC) in this situation, is the slip dissolution model (also called the film rupture or slip-oxidation model). In this model, the propagation of cracks is mainly due to the rupture of a passive film at the crack tip. In the initial state, the passive film forms over the crack faces and at the crack tip. SCC results from the dynamic synergy between passive film formation, crack tip strain rate, depassivation, repassivation...The slip dissolution model postulates that the rupture of passive film at the crack tip is due to the local dynamic plastic strain; this process allows the dissolution of metal in this region and provides the advance of cracks. The main ideas of this model are illustrated in Figs. 3,4. Crack velocity in this case is directly related to the rate of metal dissolution. However, this assumption leads to consider another aspect that is repassivation of the crack faces. The works of Scully (1971, 1972, 1980) proposed that crack propagation can only be observed when re-passivation rate and crack tip strain rate are close.

The slip dissolution model can be divided into three steps: (S1) the crack tip is covered by the passive film and the loading is applied; (S2) the rupture of the passive film occurs when the strain rate reaches a threshold value, then metal dissolution at the crack tip takes place and crack propagation occurs; (S3) the passive film is reformed. The detail of these steps are illustrated in Fig. 3

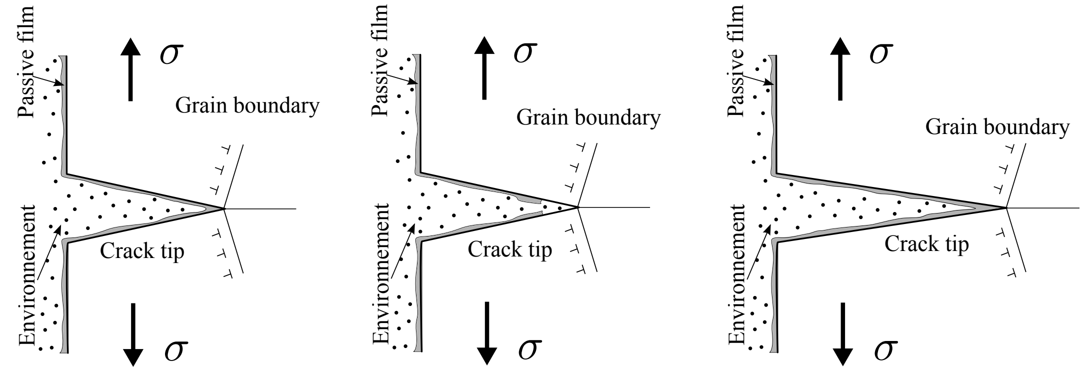

① Passive state of the crack flanks ② Dissolution and propagation ③ Repassivation

Figure 3: Three steps of crack propagation in the slip dissolution model provided by stress corrosion cracking by anodic dissolution

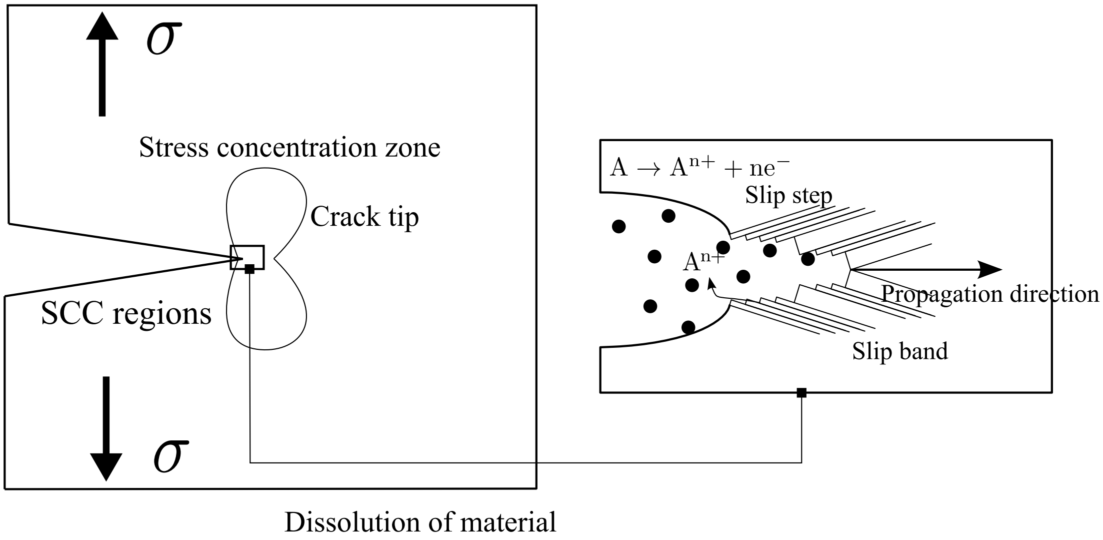

Figure 4: Description of chemi-mechanical phenomena of stress corrosion cracking by slip dissolution at crack tip

Four main "postulates" can be enhanced and re-inserted in the model that will be developed in this work. (i) *the strain rate can be considered as the rate-limiting step of SCC in this system due to the rupture of the* *passive film at the crack tip* (**P1**). At higher strain rate, the time available for corrosion process to develop is too short and the ductile fracture remains predominant. At lower strain rate, the passive film at crack tip doesn't fail and dissolution of the metal at the crack tip is inhibited. So, ductile failure due to insufficient corrosion is observed.

At a smaller scale, SCC is related to the micro-structure of the material as dissolution occurs preferentially within specific features, for example along the grain boundaries (see Fig. 3,4). Because they are areas of high energy, many impurities segregate to them, and they are a preferential site for precipitation of carbides. However, in this work, the macroscopic scale (the scale of the homogeneous material) is used. Hence, (ii) *only the SCC at the crack tip will be considered* (**P2**).

On the other hand, the experimental observations show that, SCC cracks present a ratio between crack length and crack opening that can be found within the range 100 to 1000, some time above 1000. This result means that, when the crack propagates, the crack faces are expected to show neither corrosion nor plastic deformation. Moreover, we observe no stress appearing in these regions (crack faces), whereas a high-stress concentration is found at the crack tip. Thus, (iii) *the environment is in contact with a material over a short distance close to the crack tip* (**P3**).

In addition, one has to make a difference between material points along the crack front that are located on the specimen surface (in direct contact with the solution) or in the bulk material. It provides (iv) *the different in-*

fluences of SCC on the crack tip with respect to the depth (**P4**). This aspect have to be accounted for in the model.

Simulation of slip dissolution induced SCC is an open question in the literature. The mechanical properties of the passive films forming on the specimen surface are difficult to obtain. Therefore the simulation of film rupture is not possible. In this work, we propose a new way to model our four principal points (P1,P2,P3 and P4) of SCC processes, in which corrosion occurs when the dynamic at crack tip (called activated crack) satisfies a condition related to strain rate (introduced in the next section). SCC provides here the removal of material, so the control volume just ahead of crack tip is softening. Consequently, crack propagation occurs at a stress intensity factor K_{ISCC} below the fracture toughness K_{IC} or at a stress σ_{SCC} below the ultimate tensile stress σ_C.

4. Modeling

4.1. Description of film rupture phenomena by using diffusion of degradation

In this subsection, we propose a model to describe the influence of film rupture on the fracture problem. As discussed above, the major impact of slip dissolution is the change of the material behavior. In more details, material embrittlement occurs and reduces the resistance of material. To introduce these phenomena in the modeling, we use here a diffusion model to describe the evolution of the softening of material around the crack tip.

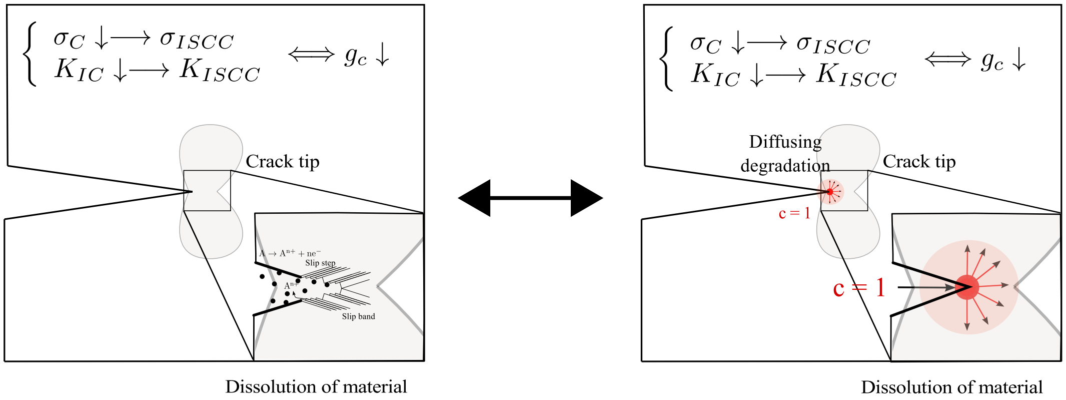

Figure 5: Description of the influence of slip dissolution on fracture mechanics by using an equivalent model based on diffusion of degradation

In the activated crack, i.e when the crack tip strain rate is higher than a critical value, the passive film fails. Then, with the presence of chemical products and SCC conditions in this region, the dissolution of the material occurs. However, modeling these phenomena by using numerical simulations is not straightforward, so we use here another way: *the dissolution of material is replaced by the diffusing degradation c.* In addition, the criterion of strain rate $\dot{\boldsymbol{\varepsilon}}$ (see **P1**) is replaced by the crack propagation rate $\dot{d}$ because the definition of strain at the crack tip is a difficult question.

The main idea of the proposed model is depicted in Fig. 5. We describe here the equivalent meaning of the two models that yields a pronounced softening behavior of material at the crack tip (due to the slip dissolution or the appearing of “micro-cracks”).

The distribution of the diffusing degradation is described by using the

Fick's laws of diffusion. The first law states that the diffusing degradation flux $\mathbf{q}$ is proportional to the diffusing concentration gradient. $\mathbf{q}$ represents the source of SCC (slip dissolution in the crack tip) that induces the propagation of "micro-cracks" or material degradation. In mathematical terms this can be expressed as:

$$\mathbf{q} = -\mathbf{D}(\mathbf{x})\nabla c \tag{1}$$

where $\mathbf{D}(\mathbf{x})$ is the diffusion coefficient and ∇ is the gradient operator.

Fick's second law relates the diffusing flux $\mathbf{q}$ at a given point to its degradation rate by means of the equation

$$\frac{\partial c}{\partial t} = -\nabla \mathbf{q} \tag{2}$$

We apply this principle only for activated crack tips (see **P2,3**), i.e. we impose $c = 1$ at the crack tip by using Dirichlet boundary conditions and then the diffusion problem is solved for the whole sample. Note that the crack tips are updated for each time steps corresponding to crack propagation.

Following (**P4**), the influence of film rupture phenomena in the surface and within the volume are different, that provides the tendency of crack propagation preferentially on the surface. To model this effect, we use here an in-homogeneous diffusion coefficient, i.e depending on the depth. We present an example of a structure containing a semi elliptical crack (see Fig. 6) subjected to SCC. The degradation coefficient is taken $\mathbf{D}(\mathbf{x}) = \mathrm{D}_0$ in the surface, and $\mathbf{D}(\mathbf{x})$ is a monotonically increasing function of depth ($\mathbf{x}$ in

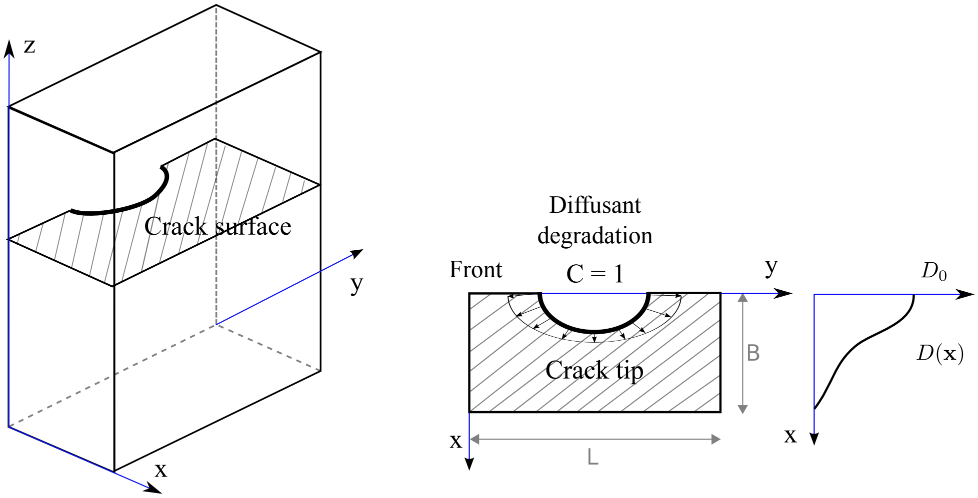

Figure 6: Slip dissolution phenomena at crack tip: distribution of diffusing degradation for the case of structure containing a semi elliptical crack

this case). From these properties, we can construct a simple solution for this example:

$$\begin{cases} \mathrm{D}(\mathbf{x}) = \mathrm{D}_0 \quad \forall \mathbf{x} \in \partial\Omega_{x=0} \\ \\ \mathrm{D}(\mathbf{x}) = \mathrm{D}_0 \left(\dfrac{B-x}{B} \right)^m \quad \forall \mathbf{x} \in \Omega / \partial\Omega_{x=0} \end{cases} \tag{3}$$

Where the coefficient $m \geqslant 2$

For an in-homogeneous isotropic medium, ($\mathbf{D}(\mathbf{x})$ depends only on the position $\mathbf{x}$) the diffusion equation is rewritten as

$$\frac{\partial c}{\partial t} = \mathrm{D}(\mathbf{x}) \triangle c + \sum_{i=1}^{3} \frac{\partial \mathrm{D}(\mathbf{x})}{\partial x_i} \frac{\partial c}{\partial x_i} \tag{4}$$

For more complex sample geometries, a levelset function (the distance to the surface in contact with the aggressive medium) is used to compute the value of **D** at any point inside the sample. To model macroscopic material embrittlement, the fracture toughness g_c directly depends on the diffusing degradation. The increasing of c induces the decreasing of g_c. However, when full diffusing degradation occurs ($c = 1$), the material is still resistant, thus g_c should not vanish for $c = 1$. We define the relation between g_c and c by the following expression:

$$g_c = \left[(1 - k_c)\,(1 - c)^n + k_c\right].g_c^0 \tag{5}$$

An example of this typical function is depicted in Fig. 7, for several values of $n = 2, 3, 6$. We use here $k_c = 10\%$, i.e for $c = 1$, 10% of the material resistance remains.

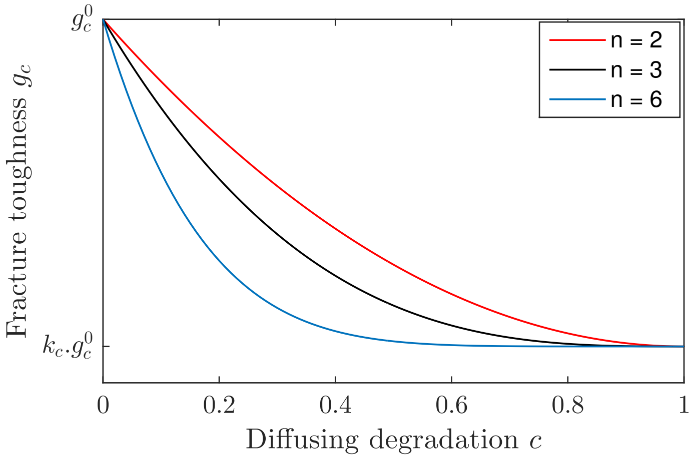

Figure 7: Influence of diffusing degradation on the fracture toughness

4.2. Phase field modeling of stress corrosion cracking

In the following, the basic concepts of the phase field method are briefly summarized. For more details and practical implementation aspects, the interested reader may refer to Miehe et al. (2010); Nguyen et al. (2015). The phase field method is based on a regularized formulation of a sharp crack description. A regularized variational principle describing both the evolution of the mechanical problem and of an additional field d describing the damage (called phase field), is discretized by a finite element procedure and a staggered algorithm. The method alleviates the shortcomings of re-meshing crack geometry by using a fixed mesh and a regularized description of the discontinuities. In addition, crack initiation can be modeled in a straightforward manner. In contrast to volume damage models, usually implemented in non-linear codes, such regularized approach is directly connected to the brittle failure theory of crack propagation. In the present work, the phase field method has been implemented in a house-made code both in 2D and 3D.

In the phase field method, assuming small strains, the regularized form of the energy describing the cracked structure is expressed by:

$$E(\mathbf{u}, d) = \int_{\Omega} W_u(\boldsymbol{\varepsilon}(\mathbf{u}), d) d\Omega + \int_{\Omega} g_c(\mathbf{x}, \tau)\gamma(d, \nabla d) d\Omega, \tag{6}$$

where $\boldsymbol{\varepsilon}$ is the linearized strain tensor, W_u is the elastic strain energy density, depending on the displacements $\mathbf{u}(\mathbf{x})$ and on the phase field $d(\mathbf{x})$ describing the damage of the solid. g_c is a function of the fracture toughness at initial state g_c^0 and the diffusing degradation c. Note that, the irreversibility condition is applied for the fracture toughness, by the following expression:

$$g_c(\mathbf{x}, t) = \underset{\tau \in [0,t]}{min} \left\{ g_c \left(g_c^0, c(\mathbf{x}, \tau) \right) \right\}. \tag{7}$$

For the sake of simplicity, we write $g_c = g_c(\mathbf{x}, \tau)$. In (6) , $\gamma(d, \nabla d)$ is the crack density function per unit volume (see e.g. Miehe et al. (2010); Nguyen et al. (2015)), defined by:

$$\gamma(d, \nabla d) = \frac{1}{2l} d^2 + \frac{l}{2} \nabla d \cdot \nabla d, \tag{8}$$

where l is the regularization parameter. l can be considered as a pure numerical parameter of the regularized model of brittle fracture or seen as a real material parameter for a gradient damage model. In the first case, it is recommended to take l as small as possible to better approximate brittle fracture, with regards to the size of the mesh. In the second case, l should be identified from experimental data. Such analysis with experimental validations has been recently published in Nguyen et al. (2016). It is demonstrated that this kind of regularized model *converge* to the brittle failure theory when l vanishes. In the case considered herein when g_c is heterogeneous, this *convergence* is maintained if l is smaller than the shortest wave length of the g_c field. It will checked latter on that this condition is satisfied and thus that the ability of the phase field model to approximate brittle failure is effective.

The total energy is then rewritten as $E = \int_\Omega W d\Omega$ with

$$W = W_u(\boldsymbol{\varepsilon}(\boldsymbol{u}), d) + g_c \gamma(d, \nabla d) \tag{9}$$

The unilateral contact formulation following the work of Miehe et al. (2010) is chosen to ensure damage induced by traction only, (assuming isotropic elastic behavior of the body) through:

$$W_u(\mathbf{u}, d) = \Psi^+(\boldsymbol{\varepsilon}(\mathbf{u})) \{g(d) + k\} + \Psi^-(\boldsymbol{\varepsilon}(\mathbf{u})). \tag{10}$$

With

$$\Psi^+(\boldsymbol{\varepsilon}) = \frac{\lambda}{2} \left(\langle Tr(\boldsymbol{\varepsilon}) \rangle_+ \right)^2 + \mu Tr \left\{ \left(\boldsymbol{\varepsilon}^+ \right)^2 \right\}, \tag{11}$$

$$\Psi^{-}(\boldsymbol{\varepsilon}) = \frac{\lambda}{2}\left(\langle Tr(\boldsymbol{\varepsilon})\rangle_{-}\right)^2 + \mu Tr\left\{\left(\boldsymbol{\varepsilon}^{-}\right)^2\right\}, \tag{12}$$

where ε^{+} and ε^{-} are the extensive and compressive modes of strain field $\boldsymbol{\varepsilon} = \boldsymbol{\varepsilon}^{+} + \boldsymbol{\varepsilon}^{-}$. In (11), (12) $\langle x\rangle_{+} = (x + |x|)/2$ and $\langle x\rangle_{-} = (x - |x|)/2$. The degradation function $g(d)$ in Eq. (10) is assumed to have the simple form:

$$g(d) = (1-d)^2 + k. \tag{13}$$

The function $g(d)$ has been chosen such that $g'(1) = 0$ to guarantee that the strain energy density function takes a finite value as the domain is locally cracked (see e.g. Braides (1998)) and $g(0) = 1$ to guarantee that the material is initially undamaged. $g(1) = 0$ is the limit for fully damaged material. The small parameter $k << 1$ is introduced to maintain the well-posedness of the system for partially broken parts of the domain Miehe et al. (2010).

In the following, a crack phase field evolution law is derived that can guarantee the irreversibility of the process. Assuming isothermal processes, without external micro forces, the reduced form of the Clausius-Duhem inequality is written as (see Nguyen et al. (2015) for more details):

$$\mathcal{A}\dot{d} \geq 0, \tag{14}$$

where $\mathcal{A} = -\frac{\delta W}{\delta d} = -\frac{\partial W}{\partial d} + \nabla.\left(\frac{\partial W}{\partial \nabla d}\right)$ is the variational derivative of W with respect to the phase field d. At this stage, a threshold function $F(\mathcal{A})$ such that

$$F(\mathcal{A}) \leq 0 \tag{15}$$

is introduced. Assuming the principle of maximum dissipation then requires the dissipation $\mathcal{A}\dot{d}$ to be maximum under the constraint (15). Using the method of Lagrange multipliers and the following Lagrangian:

$$\mathcal{L} = -\mathcal{A}\dot{d} + \lambda F(\mathcal{A}), \tag{16}$$

yields the Kuhn-Tucker equations:

$$\frac{\partial \mathcal{L}}{\partial \mathcal{A}} = 0, \quad \lambda \geq 0, F \leq 0, \lambda F = 0. \tag{17}$$

The first equality in (17) gives:

$$\dot{d} = \lambda \frac{\partial F(\mathcal{A})}{\partial \mathcal{A}}. \tag{18}$$

Without loss of generality, the threshold function $F(\mathcal{A})$ is assumed in the form $F(\mathcal{A}) = \mathcal{A}$. From (18) and using the second inequality in (17), we obtain:

$$\dot{d} = \lambda \geq 0 \tag{19}$$

For $\dot{d} > 0$, and from (14), (19) and the third equality in (17), which give $F = 0$, implying:

$$F = -\frac{\delta W}{\delta d} = -\frac{\partial W_u(\mathbf{u}, d)}{\partial d} - g_c \delta\gamma(d, \nabla d) = 0. \tag{20}$$

With (see e.g. Miehe et al. (2010)):

$$\delta\gamma(d, \nabla d) = \frac{d}{l} - l\Delta d \tag{21}$$

From (10), (13) and (20) we obtain

$$2(1-d)\Psi^{+} - g_c \delta\gamma(d, \nabla d) = 0 \tag{22}$$

that is the evolution law for the phase field d. As $2(1-d)\Psi^+ \geq 0$, then

$$\delta\gamma(d, \nabla d) \geq 0. \tag{23}$$

We can thus check that due to (23), the variation of crack length:

$$\dot{\Gamma}_l = \int_\Omega \delta\gamma(d, \nabla d)\dot{d}d\Omega \geq 0, \tag{24}$$

satisfying irreversible evolution of cracks.

The strain energy density function $\mathcal{H}(t)$ is introduced to describe a dependence on history Miehe et al. (2010) and to make possible loading-unloading. In this work, this function can be defined by the following:

$$\mathcal{H}(\mathbf{x}, t) = \underset{\tau\in[0,t]}{max} \left\{ \frac{l}{g_c}\Psi^+(\mathbf{x}, \tau) \right\}, \tag{25}$$

which is substituted to Ψ^+ in (22) and using (21) it yields the following phase field problem to be solved to evaluate the field $d(\mathbf{x}, t)$ at time t:

$$\begin{cases} 2(1-d)\mathcal{H} - \{d - l^2\Delta d\} = 0 \ \text{ in } \Omega, \\ d(\mathbf{x}) = 1 \ \text{ on } \Gamma, \\ \nabla d(\mathbf{x}) \cdot \mathbf{n} = 0 \ \text{ on } \partial\Omega, \end{cases} \tag{26}$$

5. Numerical formulation and algorithm

5.1. Diffusion problem

The strong form defined in (2) can be expressed as:

$$\frac{\partial c}{\partial t} + \frac{\partial q_i}{\partial x_i} = 0 \tag{27}$$

where q_i represents the components of the flux vector expressed in an orthonormal basis with coordinates x_i. The corresponding boundary conditions are given by

$$\begin{cases} c(\mathbf{x}) = \overline{c} & \text{with } \mathbf{x} \in \partial\Omega_1 \\ q_i(\mathbf{x}) = \overline{q}_i & \text{with } \mathbf{x} \in \partial\Omega_2 \\ \partial\Omega_1 \cup \partial\Omega_2 = \partial\Omega & \text{and } \partial\Omega_1 \cap \partial\Omega_2 = \emptyset \end{cases} \tag{28}$$

Multiplying the strong form by a test function δc and integrating over Ω, we obtain:

$$\int_\Omega \left\{ \delta c \frac{\partial c}{\partial t} + \delta c \frac{\partial q_i}{\partial x_i} \right\} d\Omega = 0. \tag{29}$$

where δc satisfy:

$$\int_\Omega \frac{\partial \delta c}{\partial x_i} d\Omega < \infty \quad \text{and} \quad \delta c = 0 \text{ on } \partial\Omega_1 \tag{30}$$

Using the integral by parts and the divergence theorem, we finally obtain:

$$\int_\Omega \left\{ \delta c \frac{\partial c}{\partial t} - \frac{\partial \delta c}{\partial x_i} q_i \right\} d\Omega + \int_{\partial\Omega} \delta c q_i n_i dS = 0. \tag{31}$$

5.2. Phase field problem

Starting from $(26)_1$, multiplying by a test function δd and integrating over Ω, we obtain:

$$\int_\Omega \left\{ 2(1-d)\mathcal{H}\delta d - \left(d - l^2 \Delta d\right) \delta d \right\} d\Omega = 0. \tag{32}$$

Using the property:

$$(\Delta d)\ \delta d = \nabla \cdot (\nabla d \delta d) - \nabla d \cdot \nabla(\delta d) \tag{33}$$

and the divergence theorem, Eq. (32) is rewritten as:

$$\int_{\Omega} \{2(1-d)\mathcal{H} - d\}\, \delta d - \int_{\Omega} l^2 \nabla d \cdot \nabla(\delta d)\ d\Omega$$

$$+ \int_{\partial\Omega} l^2 \nabla d \cdot \mathbf{n} \delta d\ d\Gamma = 0 \tag{34}$$

Using (26_3), we finally obtain:

$$\int_{\Omega} \left\{ (2\mathcal{H} + 1)\, d \delta d + l^2 \nabla d \cdot \nabla(\delta d) \right\} d\Omega = \int_{\Omega} 2\mathcal{H} \delta d d\Omega. \tag{35}$$

In the present work, the computations are performed in quasi-static conditions. Then, the time steps introduced in the following actually refer to load increments. Introducing a time stepping, the problem to be solved at time t^{n+1} is expressed by seeking $d(\mathbf{x}) \in \mathcal{S}_d$, such that:

$$\int_{\Omega} \left\{ (2\mathcal{H}_n + 1)\, d_{n+1} \delta d + l^2 \nabla d_{n+1} \cdot \nabla(\delta d) \right\} d\Omega = \int_{\Omega} 2\mathcal{H}_n \delta d d\Omega.$$

$$\forall \delta d(\mathbf{x}) \in H^1_0(\Omega). \tag{36}$$

where $\mathcal{H}_n = \mathcal{H}(\mathbf{u}_n)$ and the fracture toughness g_{cn} are computed from the previous time step (load increment) by:

$$\begin{cases} g_{cn}(\mathbf{x}) = g_{cn}\left(g_c^0, c_n(\mathbf{x})\right) & \text{if } g_{cn}(\mathbf{x}) \leq g_{cn-1}(\mathbf{x}), \\ g_{cn}(\mathbf{x}) = g_{cn-1}\left(g_c^0, c_n(\mathbf{x})\right) & \text{if } g_{cn}(\mathbf{x}) > g_{cn-1}(\mathbf{x}). \end{cases} \tag{37}$$

and

$$\begin{cases} \mathcal{H}_n(\mathbf{x}) = \dfrac{l}{g_{cn}} \Psi_n^+(\mathbf{x}) & \text{if } \Psi_n^+(\mathbf{x}) > \Psi_{n-1}^+(\mathbf{x}), \\ \\ \mathcal{H}_n(\mathbf{x}) = \dfrac{l}{g_{cn}} \Psi_{n-1}^+(\mathbf{x}) & \text{if } \Psi_n^+(\mathbf{x}) \leq \Psi_{n-1}^+(\mathbf{x}). \end{cases} \tag{38}$$

Note that Eqs. (38),(37) is the algorithmic counterpart of Eqs. (25), (7).

5.3. Displacement problem

The weak form associated with the displacement problem is found by solving the variational problem:

$$\mathbf{u}(\mathbf{x}) = Arg\left\{\inf_{\mathbf{u}\in\mathcal{S}_u}\left(E(\mathbf{u},d) - W^{ext}\right)\right\} \tag{39}$$

where $\mathcal{S}_u = \{\mathbf{u}|\mathbf{u}(\mathbf{x}) = \bar{\mathbf{u}} \text{ on } \partial\Omega_u, \ \ \mathbf{u}\in H^1(\Omega)\}$ and $W^{ext} = \int_\Omega \mathbf{f}\cdot\mathbf{u}d\Omega + \int_{\partial\Omega_F}\overline{\mathbf{F}}\cdot\mathbf{u}d\Gamma$ with $\mathbf{f}$ and $\overline{\mathbf{F}}$ body forces and prescribed traction over the boundary $\partial\Omega_F$. We obtain the classical weak form for $\mathbf{u}(\mathbf{x})\in\mathcal{S}_u$:

$$\int_\Omega \boldsymbol{\sigma} : \boldsymbol{\varepsilon}(\delta\mathbf{u})d\Omega = \int_\Omega \mathbf{f}\cdot\delta\mathbf{u}d\Omega + \int_{\partial\Omega_F}\overline{\mathbf{F}}\cdot\delta\mathbf{u}d\Gamma \ \forall\delta\mathbf{u}\in H_0^1(\Omega), \tag{40}$$

where the second-order Cauchy stress tensor $\boldsymbol{\sigma} = \frac{\partial W_u}{\partial\boldsymbol{\varepsilon}}$ is given using (10) and (13), by:

$$\boldsymbol{\sigma} = \left((1-d)^2 + k\right)\left\{\lambda\left\langle Tr\boldsymbol{\varepsilon}\right\rangle_+\mathbf{1} + 2\mu\boldsymbol{\varepsilon}^+\right\} + \lambda\left\langle Tr\boldsymbol{\varepsilon}\right\rangle_-\mathbf{1} + 2\mu\boldsymbol{\varepsilon}^-. \tag{41}$$

5.4. Crack onset by using experimental data

Using the experimental procedures introduced in section 2, we present here a typical result in Fig. 8, six steps are depicted. We recognize the crack onset at different points in the sample surface. Faults of micro-structure lead to stress concentrations in the surrounding region, in which the passive film fails and provides new crack nucleation sites. Then, crack merging is observed, and finally a continuous crack network is created, the coalescence process becomingxs an essential characteristics.

In this work, we study the fracture phenomena at meso scale. The sources (for example: the fault of micro-structure) of these phenomena come from

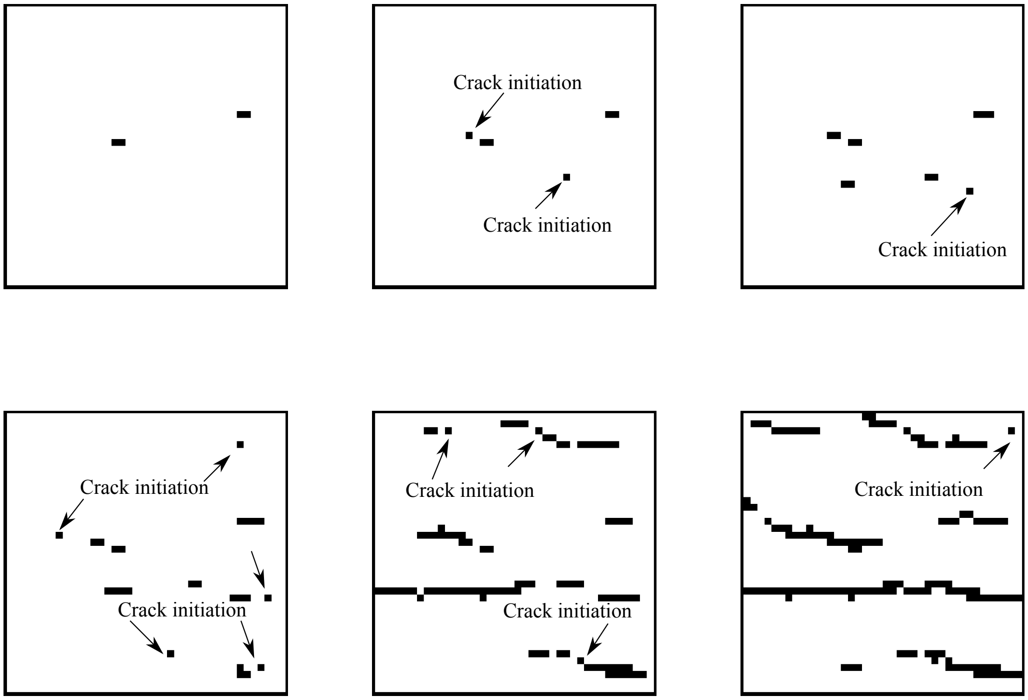

Figure 8: Crack extraction by using DIC: crack propagation for several loading steps

smaller scales. With our experimental setup, we do not have the access to micro-structural details. This lack provides the difficulties to model the initiation of cracks, also the complex trajectory of crack propagation. A solution has been proposed to treat this problem: crack initiation is assumed following experimental crack detection obtained using DIC analysis (see section 2.2). This solution is suitable for the main objective of this work: studying crack interaction phenomena.

The main idea of the method is the following: at a loading step n, experimental results are used to initiate cracks. Then, cracks are free to propagate by themselves. We present here an example in Fig. 9. At loading step 1, the structure is subjected to a prescribed displacement $\overline{\mathrm{U}}_1$. This time step shows a crack (black color) and two crack onsets, which are depicted by two blue squares in Fig. 9(a). At step 2, with a new loading (prescribed displacement $\overline{\mathrm{U}}_2$), the previously considered cracks (those of step 1) propagate and two crack onsets occur, see Fig. 9(b). Note that, this process is intrinsically modeled by the fracture model. We only prescribe the initiation of four new crack onsets (red square) by using experimental data. Similarly at step 3, the structure is subjected to new prescribed displacements $\overline{\mathrm{U}}_3$, we observe the propagation of cracks, and we also add two new crack onsets following experimental results (green square). This typical simulation gives us the evolution of cracks under loading. This result is used to study the interaction of cracks and to compare with experiments at a chosen loading.

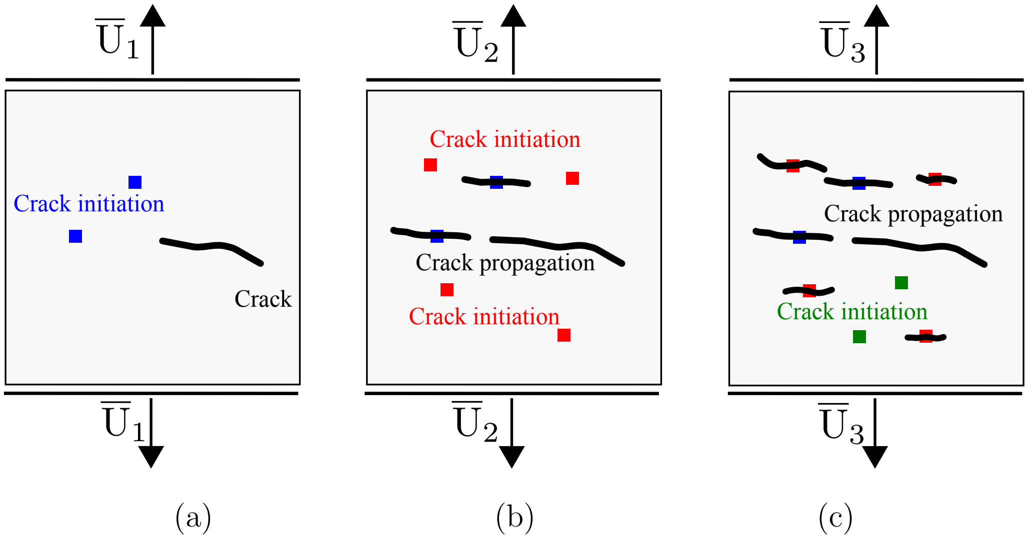

Figure 9: Crack onset by using result of DIC for three different loading steps: (a) first loading step; (b) second loading step; (c) third loading step

The initial crack can be modeled as either a discrete crack in the geometry or as an induced crack in the phase-field. However, the crack initiation is promoted by a micro-structurally induced stress concentration. When crack initiation is detected experimentally from DIC data, stress concentrations have already played their role of crack initiation precursor. By using the discontinuous geometry, the discrete crack always requires a period of time (several loading steps) to induce stress concentration, and then propagate. The propagation of cracks obtained in the simulations is thus delayed if discrete cracks are introduced at the time when they are detected experimentally. We propose here a solution to treat this issue, the crack is initiated at earlier state (for example: nucleation) by using the strain history function defined in Eq. (25). This method has been introduced in the work of Borden et al. (2012) to initiate cracks. We use this method to nucleate cracks ($d = 0.25$, see Amor et al. (2009)) in the numerical model before they can be detected experimentally.

For the induced crack nucleation, an initial strain history field is specified such that an initial crack in the phase-field is defined. To define the initial strain-history field we let L be a line that represents the discrete crack we wish to include and $DisT(\mathbf{x}, L)$ is the distance from x to the line L. The strain history field is then defined as:

$$\mathcal{H}_0(\mathbf{x}) = \begin{cases} \dfrac{d_0}{2(1-d_0)}\left(1 - \dfrac{DisT(\mathbf{x}, L)}{l}\right) & \text{for } DisT(\mathbf{x}, L) \leq l \\ \\ 0 \quad \text{for } DisT(\mathbf{x}, L) > l \end{cases} \tag{42}$$

where d_0 is the initial prescribed value of the phase field. We can use this principle to initiate cracks anywhere in the domain without reference to the mesh. This method proves highly advantageous in specifying complex surface cracks in 3D bodies. We also set the intial state of crack by defining a corresponding value for d_0 which is here set to the crack nucleation threshold, i.e $d_0 = 0.25$. Crack nucleation introduces stress concentration, providing a source to crack onset later. This mechanism is similar to stress concentrations induced by the fault in micro-structure.

However, this method requires a new parameter, that is the delay between the time to nucleate cracks and the time when they are detected from DIC data. We define Δt as the delay between crack nucleation and crack onset (observed by DIC). This parameter will be determined by using inverse analyzes (introduced in the next section). Moreover, in order to account for experimental observations (*rupture of passive films at a region in the surface provides the stress concentration and then crack nucleation*), cracks are nucluated within an finite element in the surface, and we immediately activate SCC by means of the diffusing degradation i.e. prescribing $c = 1$ at the surface nodes of this element.

5.5. Algorithm

The overall algorithm, involving the coupled SCC - damage mechanics model, is described as follows:

Initialization: Initialize the displacement field $u_0(\mathbf{x})$, the phase field $d_0(\mathbf{x})$, and the degradation field $c_0(\mathbf{x})$.

FOR all loading increments (pseudo time t_{n+1}):

```
Given $\mathbf{u}_n(\mathbf{x})$, $d_n(\mathbf{x})$ and $c_n(\mathbf{x})$:
  1. Compute phase field $d_{n+1}(\mathbf{x})$
     1.1 Update fracture toughness $g_c(\mathbf{x}, \tau)$ from (5) and (7)
     1.2 Nucleate cracks from experimental data following section 5.4
     1.3 Solve the phase field problem (36)
  2. Compute diffusing degradation field $c_{n+1}(\mathbf{x})$
     2.1 Update the crack tips
     2.2 Check crack propagation rate
            if $\dot{d} \geq \mathrm{d}_c$ at the crack tips
              Solve the diffusion problem (31)
            end
  3. Compute displacement field $\mathbf{u}_{n+1}(\mathbf{x})$
     3.1 Update the elastic parameters:
         $\mathrm{E}(\mathbf{x}) = g(d(\mathbf{x}), k)\mathrm{E}_0$ and $\nu(\mathbf{x}) = g(d(\mathbf{x}), k)\nu_0$
     3.2 Solve the displacement problem (40)
  4. $(.)_n \longleftarrow (.)_{n+1}$ and go to (1).

END
```

In this algorithm, the overall coupled problem is solved in a staggered manner. This is made possible by the use of the history function in the phase field problem. This strategy avoids iterating between the displacement and the phase field problems but the load increment has to be small enought to ensure converge of in the space-time domain.

6. Results and discussion

6.1. Benchmark test of a structure containing a semi elliptical crack

The main purpose of this first example is to consider the influence of SCC on fracture mechanics. For this aim, we consider the benchmark problem of the propagation of a semi elliptical crack. A domain whose edge lengths are $L \times B \times H = 1.0 \times 0.4 \times 1.0$ mm^3 contains an initial crack (semi elliptical form), as depicted in Fig. 10. The lower surface ($z = 0$) of the domain is constrained along z-directions, while the displacement along x, y-directions are free. On the upper surface ($z = H$), the uniform $z-$displacement $\overline{U}$ increases with time (the displacement along x, y-directions are also free). Due to this tensile loading, the semi elliptical crack propagates.

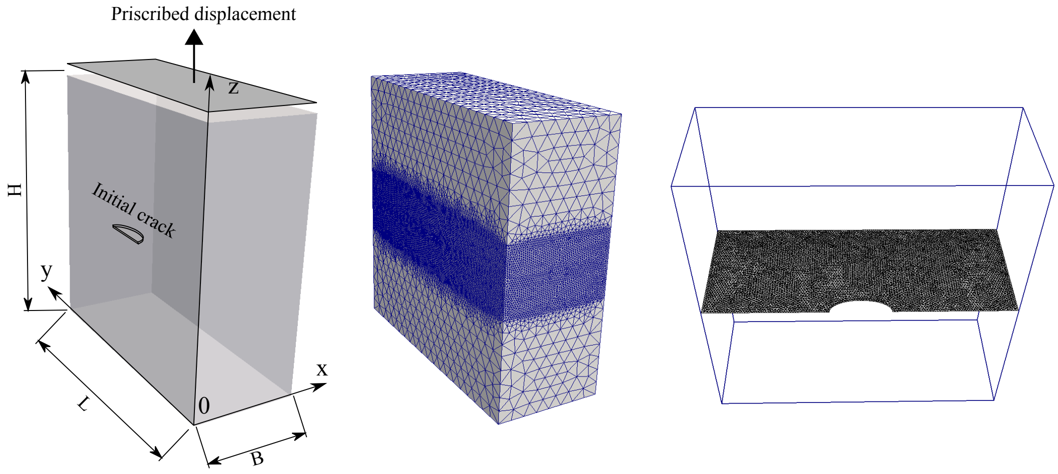

(a) (b) (c)

Figure 10: Tensile test of a structure containing a semi elliptical crack: (a) geometry and boundary conditions; (b) surface view of FEM mesh; (c) mesh view of process zone

The mesh used to model the cracked domain is refined in the expected crack propagation zone. It involves 1337605 elements as shown in Fig. 10(b). A slice of the mesh in the plane of the semi elliptical crack is depicted in Fig. 10(c). The typical size of an element in the crack propagation zone is $h_{min} \approx 5\ \mu$m. In the rest of the domain the typical mesh size is $h_{max} = 0.05$ mm.

The material is supposed to be homogeneous, elastic and isotropic with properties $E = 210$ GPa and $\nu = 0.3$ GPa. The fracture toughness is $g_c^0 = 100$ N/m, and the length scale parameter is chosen as $l = 0.01$ mm to satisfy the condition $h_{\min} \leq l/2$. Monotonic tensile displacement increments of $\Delta\overline{U} = 8.10^{-5}$ mm have been prescribed as long as $d < 0.9$ in all elements. To ensure, the convergence of the staggered scheme, we use $\Delta\overline{U} = 1.10^{-5}$mm as soon as $d > 0.9$ at one integration point.. The evolution of the crack during the simulation is shown in Fig. 11(a)(b)(c) for 3D view and Fig. 12(a)(b)(c) for a plane of investigation.

In the following, SCC will be considered through the proposed model. The parameter for diffusion is chosen as a monotonically increasing function of depth:

$$\mathrm{D}(\mathbf{x}) = \mathrm{D}_0 \left(\frac{B - x}{B}\right)^6 \tag{43}$$

The influence of diffusing degradation on the the fracture toughness is defined by the following expression:

$$g_c = \left[(1 - k_c)\,(1 - c)^3 + k_c\right].g_c^0 \tag{44}$$

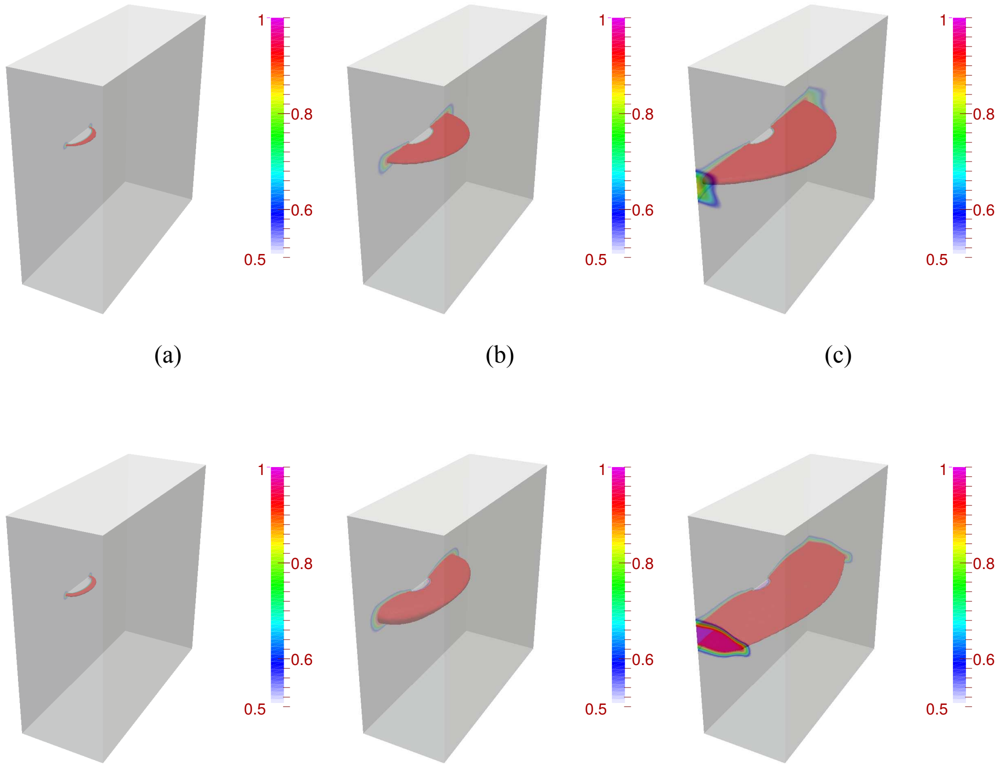

(a) (b) (c)

(d) (e) (f)

Figure 11: Tensile test of an homogeneous sample with a semi elliptical crack: the iso surface of phase field $d(\mathbf{x}) = 0.95$ is plotted. Figures (a), (b) and (c) depict the cracks onset and propagation by using the classical phase field method and correspond to $\overline{U} = 0.0031$ mm, $\overline{U} = 0.0032$ mm, and $\overline{U} = 0.0033$ mm, respectively. Figures. (d), (e) and (f) depict crack propagation for the model including both phases and SCC correspond to $\overline{U} = 0.002$ mm, $\overline{U} = 0.0022$ mm, and $\overline{U} = 0.0023$ mm, respectively.

Where $\mathrm{D}_0 = 3.10^{-3}$ mm^2/s and $k_c = 10\%$. The same loading condition is considered as in the case of purely mechanical phase field model which results are presented above. SCC at the crack tips is activated after 20 loading steps. The evolution of the crack during the simulation is shown in Figs. 11(d)(e)(f) for 3D view and Figs. 12(d)(e)(f) for a plane of investigation.

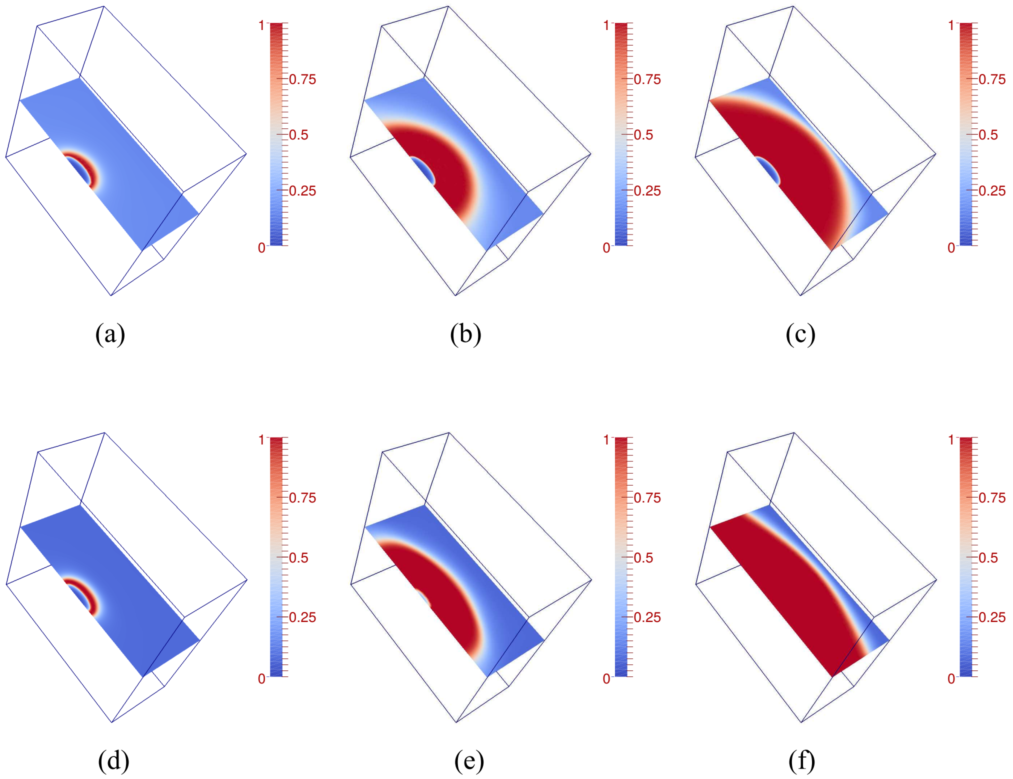

(a) (b) (c)

(d) (e) (f)

Figure 12: Crack propagation in a chosen plane ($z = 0.5H$). The phase field $d(\mathbf{x})$ is plotted. Figures (a), (b) and (c) depict the cracks onset and propagation by using the classical phase field method and correspond to $\overline{U} = 0.0031$ mm, $\overline{U} = 0.0032$ mm, and $\overline{U} = 0.0033$ mm, respectively. Figures. (d), (e) and (f) depict crack propagation for the model including both phases and SCC correspond to $\overline{U} = 0.002$ mm, $\overline{U} = 0.0022$ mm, and $\overline{U} = 0.0023$ mm, respectively.

The crack evolution predicted by the two models are strongly different (see Fig. 12). In the case of classical phase field model (purely mechanical), the propagation tendency agrees with the theory of semi-elliptic surface crack growth Newman and Raju (1981); Smith and Cooper (1989); Kikuchi and Suga (2011). Depending on the ratio of crack depth to crack length, the crack first propagates to obtain a reasonable ratio, then propagates in both directions (depth and surface) in order to keep this ratio. In the case when SCC is considered, we observe that the crack propagates in the surface more than in depth. We recognize that, the propagation tendency of crack in the SCC model is strongly dependent on the diffusing direction of degradation. The evolution of the diffusing degradation on a plane of observation is plotted in Fig. 13. Due to the expression adopted for D (see Eq. (43)), the degradation diffuses more along y-direction than along x-direction. This result reproduces very well the phenomena mentioned in experiments in the literature, that is promising for direct comparisons of cracks morphology between experiments and numerical simulations.

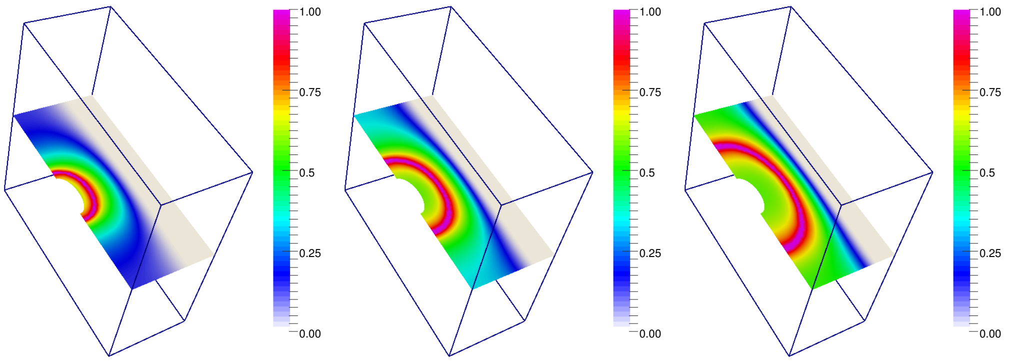

Figure 13: Observation of SCC in a chosen plane ($z = 0.5$). The diffusing degradation $c(\mathbf{x})$ is plotted. Figures (a), (b) and (c) depict the degradation correspond to $\overline{U} = 0.00205$ mm, $\overline{U} = 0.0021$ mm, and $\overline{U} = 0.00215$ mm, respectively

As mentioned above, in this frame work, the SCC is accounted by using a spatially varying fracture energy g_c, depending on the diffusing degradation. To see better this phenomenon, in Fig. 14 we plot the variation of g_c along a line of investigation located at the intersection of two planes $z = 0.5$ and $y = 0.5$. The fracture energy reaches the minimum value $g_c^{\min} = k_c g_c^0 = 10^{-5}$ kN/mm at crack tip and the maximum value $g_c^{\min} = g_c^0 = 10^{-4}$ kN/mm away from crack tip. The variation take place in a region about of 0.15 mm that is much higher than the regularization parameter $l = 0.01$ mm. This ensures that the two diffusion problems, governing the evolution of c (or g_c) and d have well separate characteristic length. The Fig. 15 plots the surface energy along the same line of investigation, for one loading step when damage has not yet occurred and three cracked steps (depicted in Fig. 13). This figure allows to check that there is no interaction between the variation of g_c which is very smooth as depicted on Fig. 14 and the phase field evolution that is related to the distribution of dissipated energy.

The stress-displacement curves obtained for both cases are depicted in Fig. 18. SCC crack propagates at a stress level below the one observed for classical case (without SCC).

In the following, we illustrate the performance of the new model in the case of constant load tests as usually performed experimentally to study SCC. Neumann boundary conditions are used in this test. The same structure as in the previous example is loaded until 80% of the critical stress, and then the load is kept constant. Then, SCC is activated. Because of the diffusing degradation, that reduces the resistance of the material, the crack propagates.

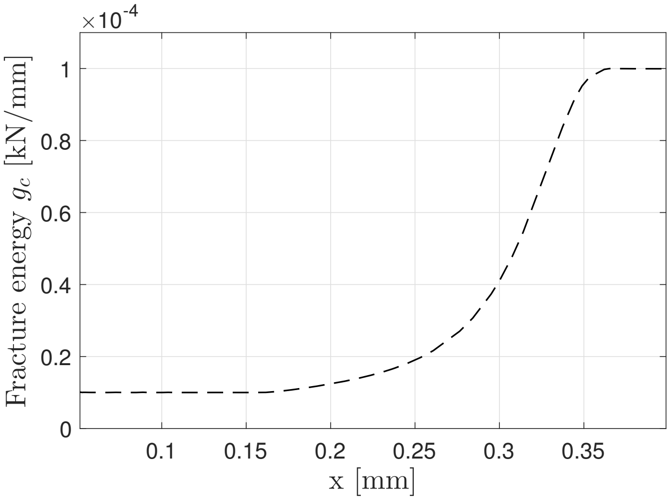

Figure 14: The influence of SCC on fracture energy: distribution of g_c along a line of investigation corresponding to $\overline{U} = 0.0021$ mm. We observe here the variation in zone about of 0.15 mm above crack tip

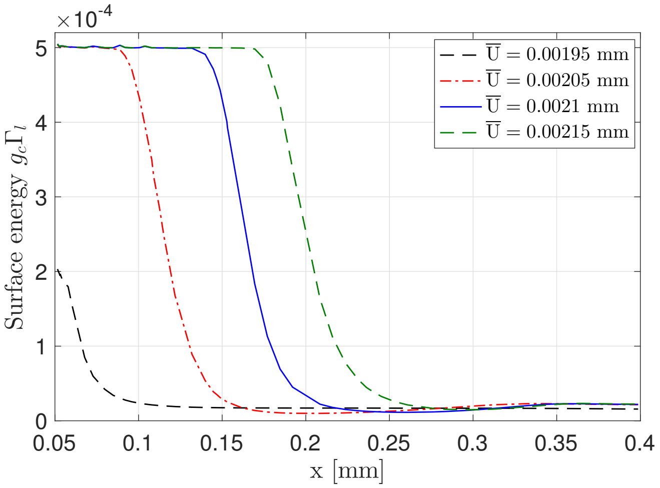

Figure 15: Evolution of surface energy along a line of investigation, corresponding to one undamaged step and three damaged steps.

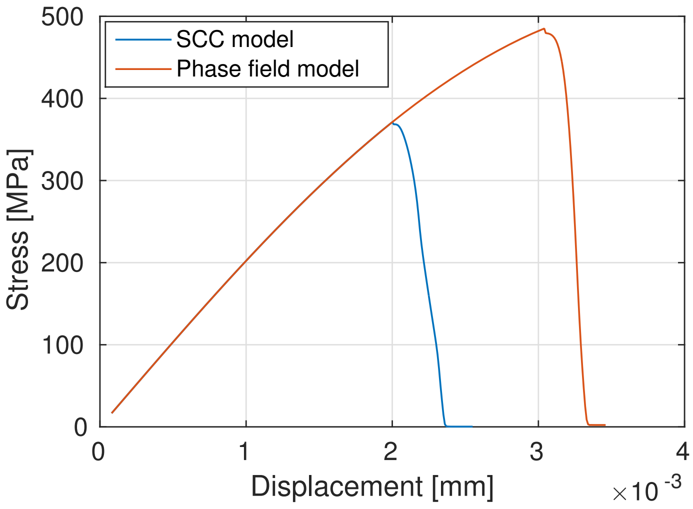

Figure 16: Comparison of stress-displacement curve for two models.

The result is depicted in Fig. 17. The stress-strain curve is plotted in Fig. **??**. This test confirms the ability of the proposed model to simulate experimental observations of SCC.

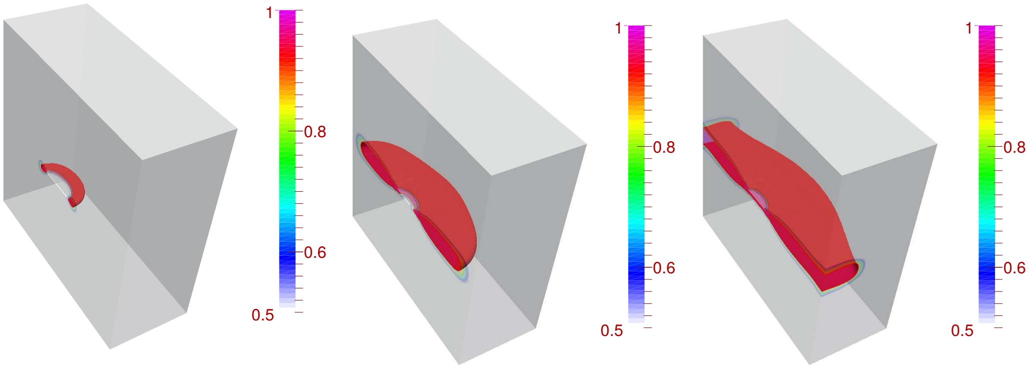

(a) (b) (c)

Figure 17: The iso surface of phase field $d(\mathbf{x}) = 0.95$ is plotted. Figures (a), (b) and (c) depict the cracks onset and propagation by using the classical phase field method and correspond to $\bar{\varepsilon}_{zz} = 0.0022$, $\bar{\varepsilon}_{zz} = 0.0025$, and $\bar{\varepsilon}_{zz} = 0.0027$, respectively

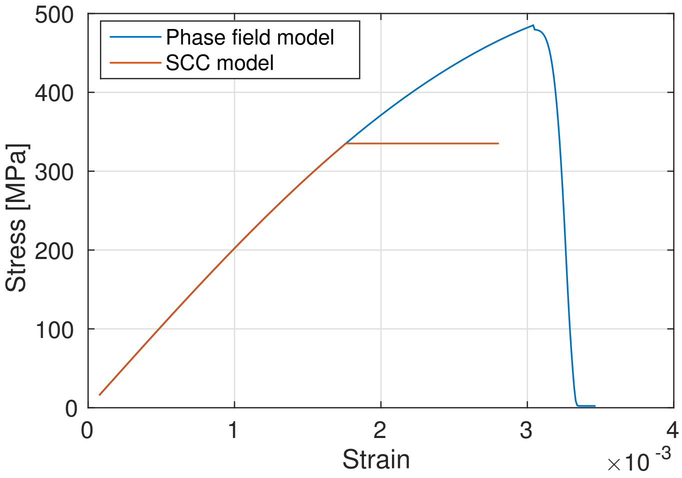

Figure 18: Stress-strain curve for SCC model subjected constant load test and comparison with classical phase field model.

6.2. Experimental validation

In this section, the crack network obtained from the experiments and the one predicted by the simulations will be compared. The proposed procedure to identify some parameters of the constitutive relations of the model is presented. This procedure is based on the inverse analysis combining experiments and simulations.

6.2.1. Identification of model parameters by inverse analysis

The elastic parameters have been taken from literature (e.g. Mills (1981); Mills and Brown (2001); Al-Rubaie et al. (2007)). We have $E = 210$ GPa and $\nu = 0.3$, the fracture toughness at initial state (without SCC) is $g_c^0 \approx 300$ N/m, the regularization length is considered as a pure numerical parameter, it is chosen corresponding to mesh size $l = 0.11$ mm. To perform the numerical simulations, some parameters are still to be defined. The first one is the diffusing degradation coefficient D_0 in Eq. (3), (we assume $m = 6$). The second parameter is the coefficient n in Eq. (5) (we use here $k_c = 1\%$). Another parameter is Δt, the delay between crack nucleation and crack onset, as discussed above in Subsection 5.4.

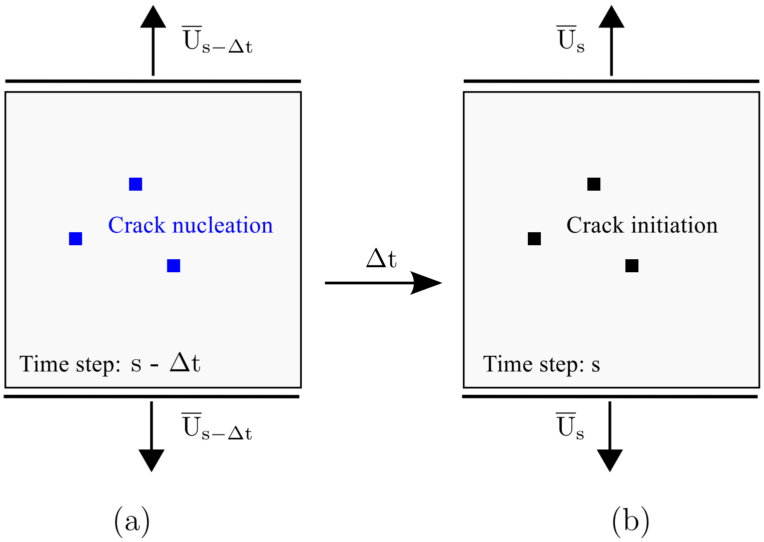

Figure 19: Main principle to define cost function of inverse analysis algorithm

For the sake of simplicity, the identification is restricted to a comparison between experimental and simulation results within a small region. The main idea is described in Fig. 19. At time step s, the experimental data allows us to know, the displacement prescribed on the boundary $\overline{\mathrm{U}}_{\mathrm{s}}$ and the initiation of several cracks, as depicted in Fig. 19(b). We perform a numerical simulation with the boundary conditions defined by DIC data until time step s. The regular mesh used for DIC is used to built a 3D mesh of 8-node elements. Note that, the crack is nucleated at time step $s - \Delta t$. In addition, the displacement field of DIC clearly shows fluctuations due to noise (see

Fig. 20). These spurious local displacement fluctuations could induce non physical damage. Hence, in order to avoid this issue, we propose to filter the DIC measurements along the sub-volume boundary at each experimental load step by a Savitzky-Golay filtering (see Orfanidis (1995)), as illustrated in Fig. 20 (black points).

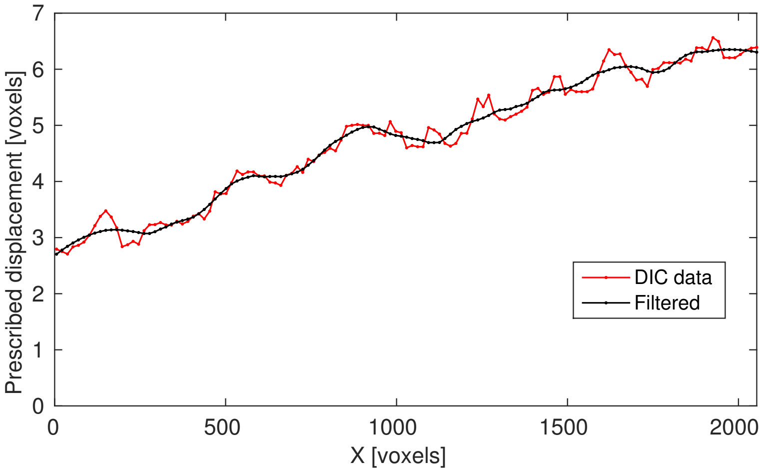

Figure 20: Displacement of boundary for an experimental load step obtained by DIC and its Savitzky-Golay filtering

The cost function to minimize for identifying the model parameters is defined as:

$$f(\mathrm{D}_0^i, n^i, \Delta t^i) = \sum_k^N \| d_k^{\mathrm{exp}} - d_k^{\mathrm{num}}(\mathrm{D}_0^i, n^i, \Delta t^i) \|^2 \tag{45}$$

Where $k = 1..N$ are the number of crack nodes obtained from experiments; $d_k^{\mathrm{exp}} = 1$, and d_k^{num} are the phase field values obtained for given $\mathrm{D}_0^i, n^i, \Delta t^i$ at the iterations i. We perform this minimization over several regions, and then take the average of the converged parameter values, we obtain: $D_0 \approx 3.32 \times 10^{-6}\text{mm}^2/\text{s}$, $n \approx 3$ and $\Delta t \approx 4800\text{s}$.

6.2.2. Surface comparison of crack morphology between numerical simulations and experiments

In the following, three sub-volumes are considered for a detailed comparison between the experimentally observed cracks from DIC processing and the numerical predictions using the proposed model.

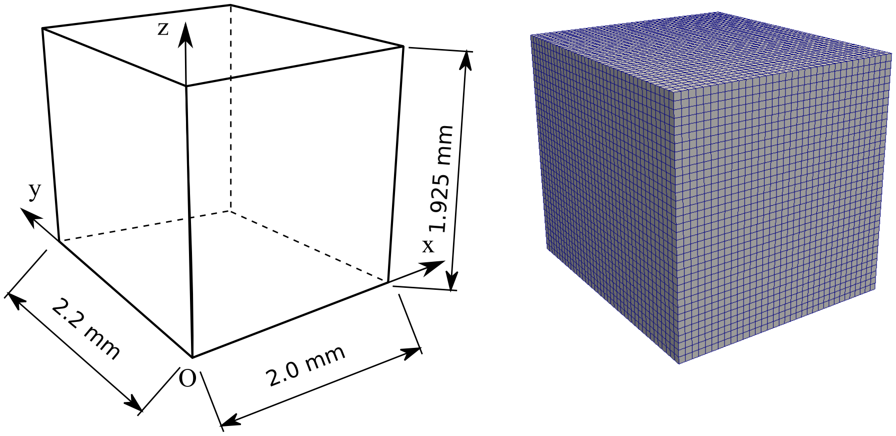

(a) (b)

Figure 21: Experimental validation, first sub-volume ($2 \times 2.2 \times 1.925$ mm^3): (a) geometry; (b) FEM mesh.

The sub-volume dimensions we first consider are $2 \times 2.2 \times 1.925$ mm^3, the material and model parameters are taken from the previous section 6.2.1. The regular mesh used for DIC is used to built a 3D mesh of 8-node elements (see Fig. 21). By this way, we can apply the same segmentation procedure on the simulation results to construct a binary map (cracked or undamaged) of elements on the sample surface. The mesh of the sub-volume consists in 50400 elements with linear interpolation. The evolving boundary conditions obtained from DIC data are applied on the boundary of the sub-volume during 95 steps. Before applying these boundary conditions both spatial and temporal interpolation and filtering as described in the previous section are used. Note that, the DIC displacement has been interpolated in time into 10 sub-increment to ensure the convergence of the staggered scheme. We compare the crack network obtained from the simulation with that one from the experiment at the same loading step. The result is depicted in Fig. 22,

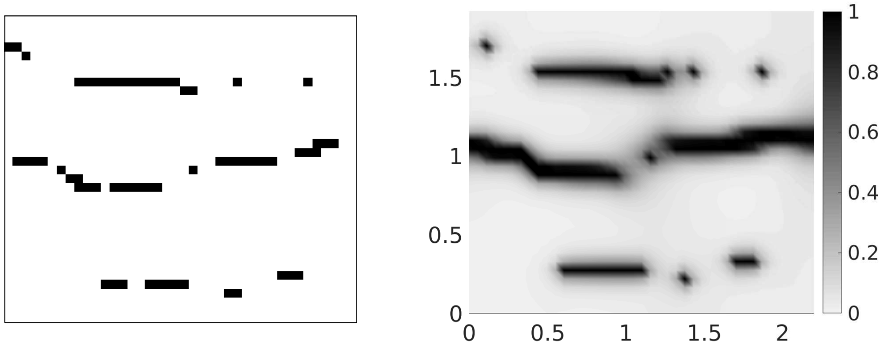

Figure 22: Comparison between experimental crack obtained from DIC procedures and from phase field method of the Inconel 600 alloy sample in sub-volume size $2 \times 2.2 \times 1.925$ mm^3, (left: experiment; right: numerical simulation.)

We perform the same analysis on other sub-volumes of different dimensions. The results are depicted in Figs. 23, 24 for two different sub-volume sizes. We obtain here a good agreement between the experiment and the

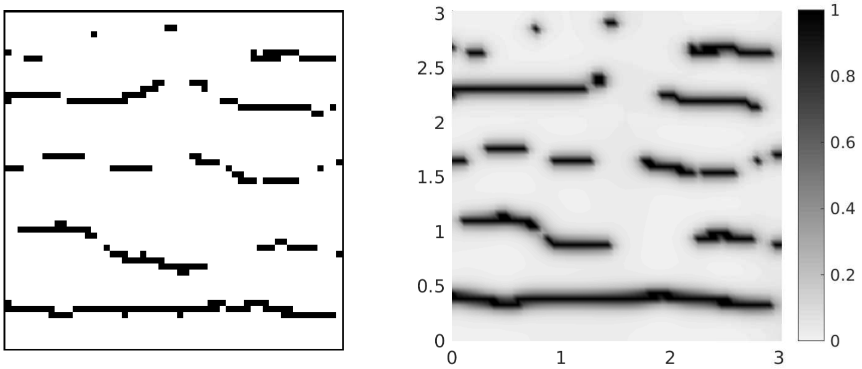

Figure 23: Comparison between experimental crack obtained from DIC procedures and from phase field method of the Inconel 600 alloy sample in sub-volume size $2 \times 3.025 \times 3.025$ mm^3, (left: experiment; right: numerical simulation.)

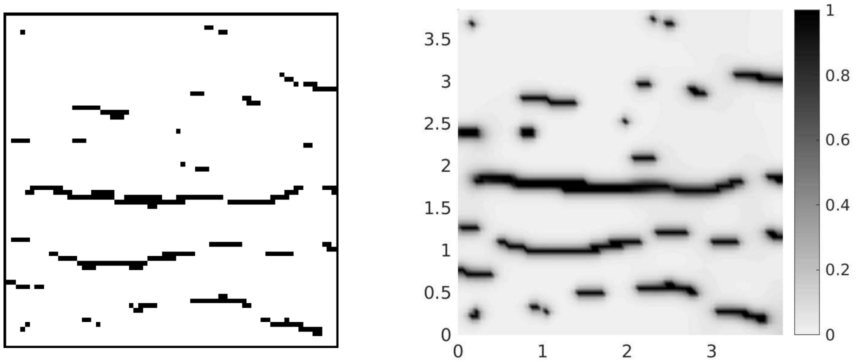

Figure 24: Comparison between experimental crack obtained from DIC procedures and from phase field method of the Inconel 600 alloy sample in sub-volume size $2 \times 3.85 \times 3.85$ mm^3, (left: experiment; right: numerical simulation.)

simulations for the three sub-volumes considered. However, we recognize that the agreement is better for the smaller size, i.e increasing structure size provides more incoherence. For a quantitative estimation of this effect, we compute the normalized inner product between the binary element map ob-

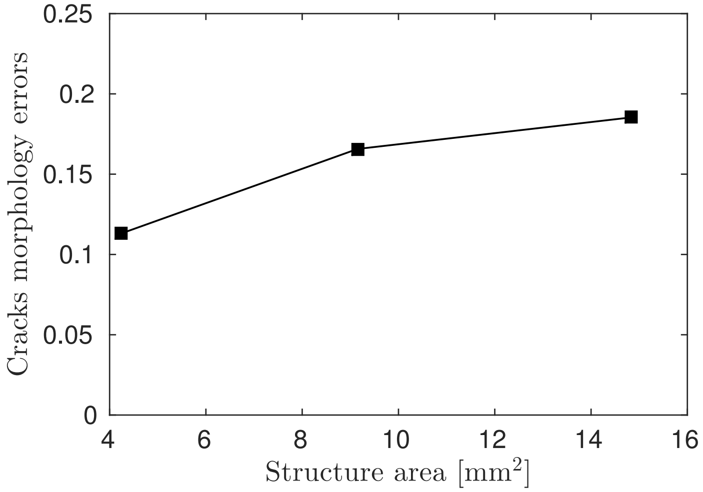

Figure 25: Error estimation of cracks morphology between experiment and predictive result from simulation

tained from DIC (called f_{exp})and that one obtained from the simulations (called f_{num}):

$$Error = 1 - \frac{\int_D \left[f_{\mathrm{exp}}.f_{\mathrm{num}}\right]\mathrm{d}\Omega}{\sqrt{\int_D f_{\mathrm{exp}}^2\mathrm{d}\Omega}.\sqrt{\int_D f_{\mathrm{num}}^2\mathrm{d}\Omega}} \tag{46}$$

This error is bounded between 0 (if f_{exp} and f_{num} are identical) and 1 (when fluctuations of f_{exp} and f_{num} are opposite). The obtained result is plotted in Fig. 25. The sub-volume size decrease induces a reduction in the problem due to lack of micro-structure details. Hence, we obtain the better agreement, i.e the crack morphology error will be smaller.

6.2.3. 3D observations of cracks morphology by using numerical simulations and comparison with experiments

In this section, we will observe the crack propagation not only on the surface, but also within the volume. Moreover, in order to demonstrate the performance of the new procedures, an finer unstructured mesh is used. The considered sub-volume dimensions are $2.2 \times 2.2 \times 2$ mm^3 (see Figs. 26), the material and model parameters are taken from the previous section 6.2.1. The mesh of the sub-volume consists in 668972 tetrahedal elements with linear interpolation (4-node elements). The mesh is refined in the vicinity of the surface $x = 0$ in contact with the aggressive solution in the experiments, as shown in Fig. 26(b). The typical size of an element in the crack propagation zone is about $h_{min} \approx 0.0225$ mm and about $h_{max} = 0.06$ mm elsewhere in the domain. Note that, the length scale l is kept to the same value as for the previous tests (in the case of regular meshes). The evolving boundary conditions obtained from DIC data are applied on the sub-volume boundary during 100 steps. Before applying these boundary conditions both spatial and temporal interpolation and filtering as described in the previous section are used.

Numerical and experimental crack propagations are compared for several loading steps. For the sake of clarity, in the 3D view ,we plot only the iso surface of phase field ($d = 0.95$). The results are presented in Fig. 29 for several loading steps. We observe the initiation of several cracks in the step presented in Fig. 29(a). In the next step, these cracks are merging and their propagation is more pronounced at the surface. A complex crack network

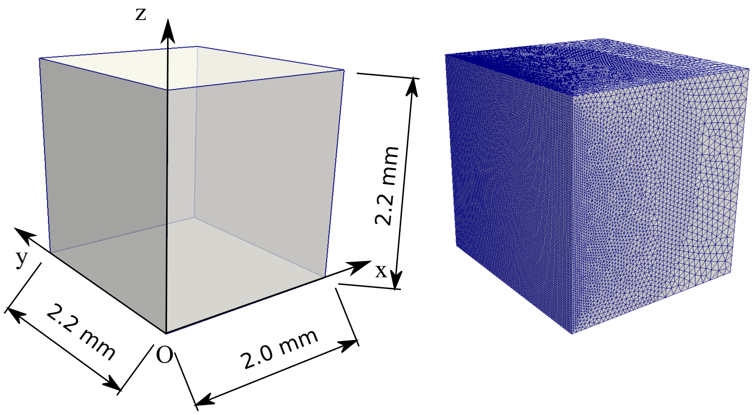

(a) (b)

Figure 26: Experimental validation, sub-volume ($2 \times 2.2 \times 2.2$ mm^3): (a) geometry; (b) FEM mesh.

with 3D crack morphology is obtained. After creating the continuous crack path at the sample surface, crack propagation occurs within the volume. These results are in very good agreement with the experimental observations. In order to perform quantitative comparisons with experiments, we plot the cracks obtained numerically at the surface $x = 0$ for several loadings. Results are compared in Fig. **??**. Remarkably we observe similar crack morphology and lengths for all three loading steps. To confirm, we compare the numerical simulation's displacement and one obtained from experiment along a line of investigation at the surface $x = 0$. The very good agreement on crack opening is obtained in Fig. 28 . One should again keep in mind that in the simulations, only initiation sites are prescribed from experimental data, there is no a priori about crack paths and the model parameters

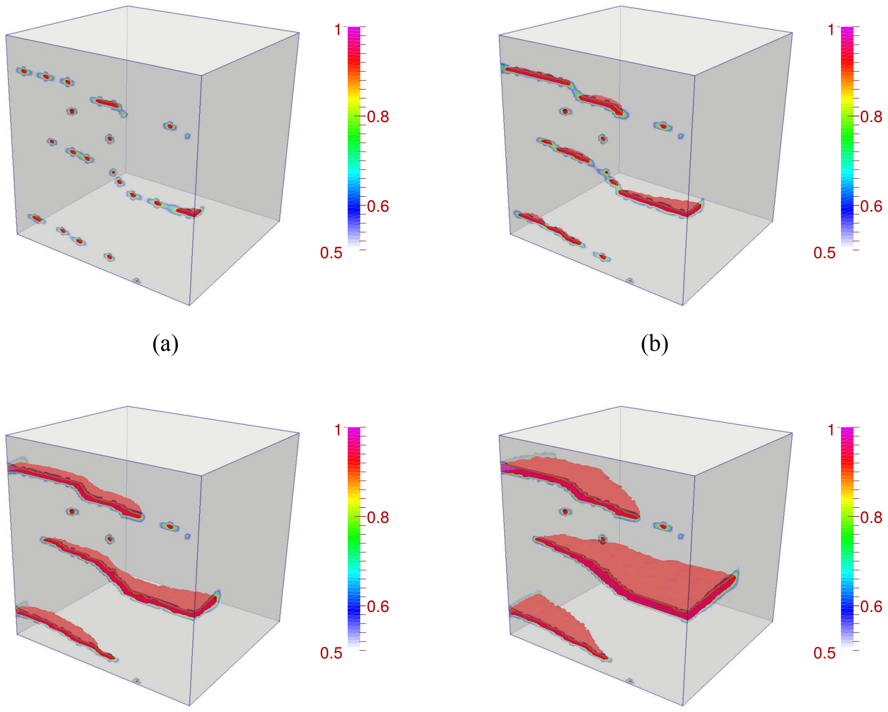

(a) (b)

(c) (d)

Figure 27: Experimental validation, sub-volume ($2 \times 2.2 \times 2.2$ mm^3): The iso surface of phase field $d(\mathbf{x})$ is plotted. Figures (a), (b), (c) and (d) depict the cracks onset and propagation corresponding to $\overline{U} = 0.014$ mm, $\overline{U} = 0.015$ mm, and $\overline{U} = 0.016$ mm, respectively.

have been identified by an inverse approach. Finally, the simulation and experiments are compared for the same load.

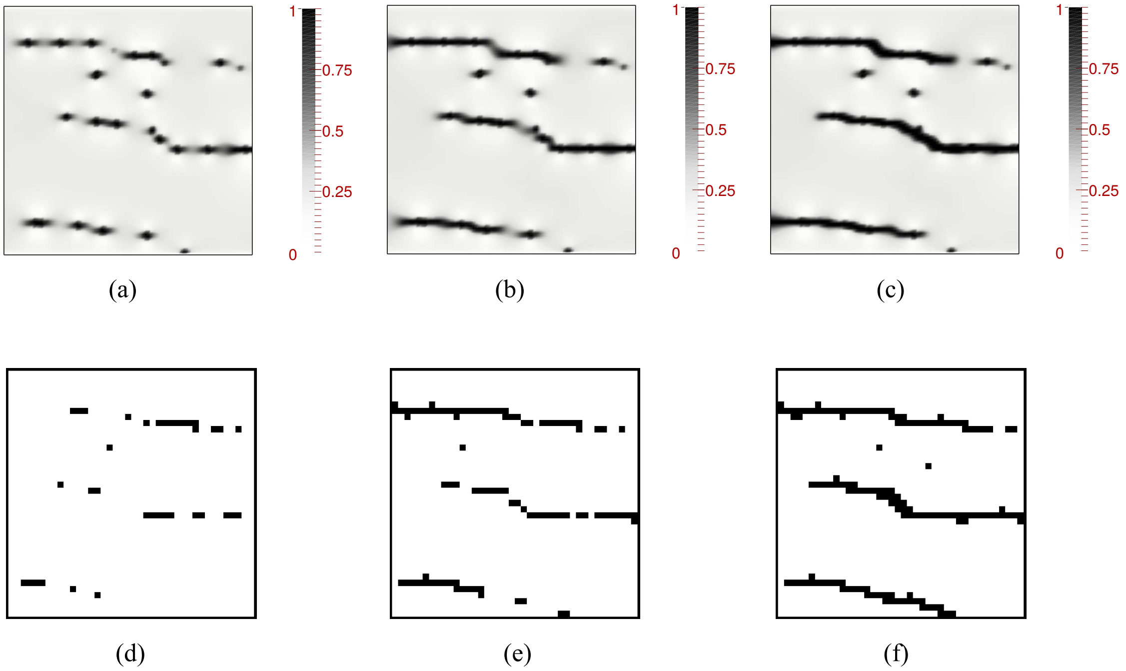

Figure 28: Comparison between experimental crack obtained from DIC procedures and from phase field method of the Inconel 600 alloy sample in sub-volume size $2 \times 2.2 \times 2.2$ mm^3, for several loading steps (bottom: experiment; top: numerical simulation.)

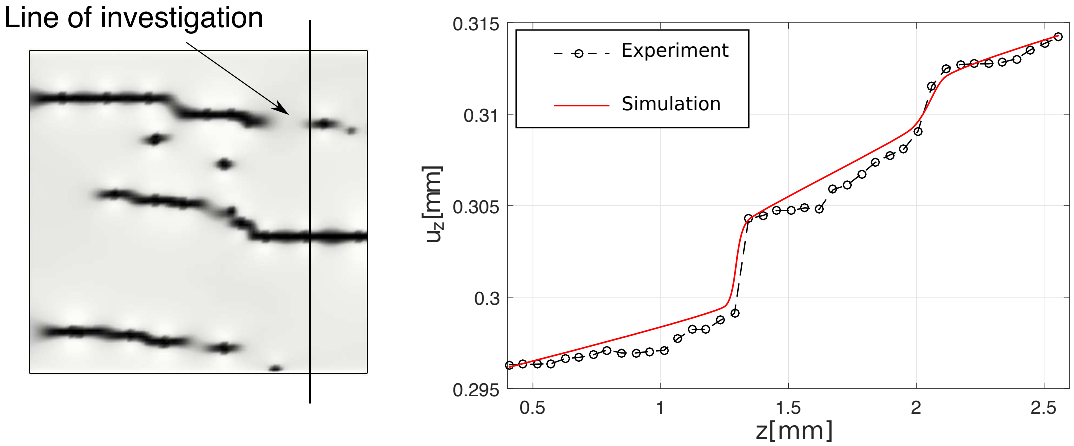

Figure 29: Comparison of local displacement between DIC measurements and numerical simulation

7. Conclusions

In this work, a new multiphysics model based on the phase field method is proposed to simulate the failure of the nickel base alloy under SCC. The slip dissolution induced SCC process is modeled by using an equivalent modeling: SCC crack growth is controlled by combining the kinetics of the diffusing degradation as an environmental factor and fracture mechanics at the crack tip.

The proposed model simulates the effects of SCC on fracture mechanics, such as crack coalescence and propagation in 3D. SCC crack initiation is strongly related to the micro-structure of the materials. In order to reproduce the crack initiation without incorporating the actual micro-structure, an approach combining simulations and experiments to nucleate cracks is carried out. This method uses the cracks onset position obtained from experimental DIC data, then imposes the strain history function in the numerical model. The cracks are then free to propagate in the numerical model, only the locations and times for crack initiation are prescribed.

Some material and model parameters are identified by an inverse approach combining experimental data and the 3D simulations. Then, they are used to perform predictive simulations. Direct comparisons between experimental results and predictions of the numerical simulation are performed ans several steps of validation are proposed. Firstly, the crack path at a chosen loading is compared and a good agreement about crack geometry and crack length are obtained. Secondly, the accurate estimation of cracks morphologies shows a very good agreement between experiments and predictions by numerical simulations. However, the lack of microstructure details still provides some incoherence when increasing the size of the analyzed structure.

The predictions provided by the proposed coupled SCC - phase field model are in good agreement with many observations of the effect on SCC by anodic dissolution crack growth. The new method opens a new way to study the SCC assisted crack coalescence and propagation. In the same direction, this model could apply for 3D experimental results, such as 3D crack morphology defined from X-ray tomography. Especially, the proposed framework become very efficient to study the case of hydrogen induced stress cracking.

8. Aknowledgements

The authors would like to acknowledge the National French Research Agency (ANR) for its financial support under contract MATETPRO ANR−12−RMNP−0020 (ECCOFIC project). The authors would like also to thank our partners AREVA, ANDRA, Institut de la Corrosion, ACXCOR and MISTRAS by their participation into the fruitful discussion during this work

References

Abhay, J., Sreekumar, K., Sinha, P., 2010. Stress corrosion cracking of high strength steel fasteners for space applications. Journal of failure analysis and prevention 10 (4), 270–281.

Al-Rubaie, K., Godefroid, L., Lopes, J., 2007. Statistical modeling of fatigue crack growth rate in inconel alloy 600. International journal of fatigue 29 (5), 931–940.

Amor, H., Marigo, J., Maurini, C., 2009. Regularized formulation of the variational brittle fracture with unilateral contact: Numerical experiments. Journal of the Mechanics and Physics of Solids 57 (8), 1209–1229.

Babout, L., Marrow, T. J., Engelberg, D., Withers, P. J., 2006. X-ray micro-tomographic observation of intergranular stress corrosion cracking in sensitised austenitic stainless steel. Materials Science and Technology 22 (9), 1068–1075.

Bellenger, F., Mazille, H., Idrissi, H., 2002. Use of acoustic emission technique for the early detection of aluminum alloys exfoliation corrosion. NDT & E International 35 (6), 385–392.

Besnard, G., Hild, F., Roux, S., 2006. 'finite-element' displacement fields analysis from digital images: Application to portevin-le châtelier bands. Experimental Mechanics 46 (6), 789–803.

Bolivar, J., Fregonese, M., Rethore, J., Duret-Thual, C., Combrade, P., 2016. Evaluation of multiple stress corrosion cracks interactions by in-situ digital image correlation. Unpublished.

Borden, M., Verhoosel, C., Scott, M., Hughes, T., Landis, C., 2012. A phase-field description of dynamic brittle fracture. Computer Methods in Applied Mechanics and Engineering 217, 77–95.

Bourdin, B., Francfort, G., Marigo, J.-J., 2000. Numerical experiments in revisited brittle fracture. Journal of the Mechanics and Physics of Solids 48 (4), 797–826.

Braides, D., 1998. Approximation of Free Discontinuity Problems. Springer Verlag: Berlin.

Choi, B., Chudnovsky, A., Sehanobish, K., 2007. Stress corrosion cracking in plastic pipes: Observation and modeling. International Journal of Fracture 145 (1), 81–88.

Ford, F., Andresen, P., 1987. Development and use of a predictive model of crack propagation in 304/316 l, a 533 b/a 508 and inconel 600/182 alloys in 288 deg c water. Environmental Degradation of Materials in Nuclear Power Systems–Water Reactors, 789–800.

Francfort, G., Marigo, J., 1998. Revisiting brittle fracture as an energy minimization problem. Journal of the Mechanics and Physics of Solids 46 (8), 1319–1342.

Hladky, K., Dawson, J., 1981. The measurement of localized corrosion using electrochemical noise. Corrosion Science 21 (4), 317–322.

Jomdecha, C., Prateepasen, A., Kaewtrakulpong, P., 2007. Study on source location using an acoustic emission system for various corrosion types. NDT & E International 40 (8), 584–593.

Karma, A., Kessler, D., Levine, H., 2001. Phase-field model of mode iii dynamic fracture. Physical Review Letters 87 (4), 045501.

Kearns, J., 1996. Electrochemical noise measurement for corrosion applications. Vol. 1277. ASTM International.

Kikuchi, M., Suga, Y. W. K., 2011. Surface crack growth simulation under mixed mode cyclic loading condition. Procedia Engineering 10, 427–432.

King, A., Johnson, G., Engelberg, D., Ludwig, W., Marrow, J., 2008. Observations of intergranular stress corrosion cracking in a grain-mapped polycrystal. Science 321 (5887), 382–385.

Kovac, J., Alaux, C., Marrow, T., Govekar, E., Legat, A., 2010. Correlations of electrochemical noise, acoustic emission and complementary monitoring techniques during intergranular stress-corrosion cracking of austenitic stainless steel. Corrosion Science 52 (6), 2015–2025.

Miehe, C., Hofacker, M., Welschinger, F., 2010. A phasefield model for rate-independent crack propagation: Robust algorithmic implementation based on operator splits. Computer Methods in Applied Mechanics and Engineering 199, 2765–2778.

Mills, W., 1981. On the relationship between stretch zone formation and the j integral for high strain-hardening materials. Journal of Testing and Evaluation 9 (1), 56–62.

Mills, W., Brown, C., 2001. Fracture toughness of alloy 600 and an en82h weld in air and water. Metallurgical and Materials Transactions A 32 (5), 1161–1174.

Newman, J., Raju, I., 1981. An empirical stress-intensity factor equation for the surface crack. Engineering Fracture Mechanics 15 (1), 185–192.

Newman, R., Healey, C., 2007. Stability, validity, and sensitivity to input parameters of the slip-dissolution model for stress-corrosion cracking. Corrosion Science 49 (10), 4040–4050.

Nguyen, T., Yvonnet, J., Bornert, M., Chateau, C., Sab, K., Romani, R., Roy, R. L., 2016. On the choice of parameters in the phase field method for simulating crack initiation with experimental validation. International Journal of Fracture 197 (2), 213–226.

Nguyen, T., Yvonnet, J., Zhu, Q.-Z., Bornert, M., Chateau, C., 2015. A phase field method to simulate crack nucleation and propagation in strongly heterogeneous materials from direct imaging of their microstructure. Engineering Fracture Mechanics 139, 18–39.

Orfanidis, S., 1995. Introduction to signal processing. Prentice-Hall, Inc.

Parkins, R., 1980. Predictive approaches to stress corrosion cracking failure. Corrosion Science 20 (2), 147–166.

Parkins, R., 1987. Current topics in corrosion: Factors influencing stress corrosion crack growth kinetics. Corrosion 43 (3), 130–139.

Richardson, J., Wood, G., 1970. A study of the pitting corrosion of al by scanning electron microscopy. Corrosion Science 10 (5), 313–323.

Saito, K., Kuniya, J., 2001. Mechanochemical model to predict stress corrosion crack growth of stainless steel in high temperature water. Corrosion Science 43 (9), 1751–1766.

Scully, J., 1971. The theory of stress corrosion cracking in alloys. North Atlantic Treaty Organization, Scientific Affairs Division.

Scully, J., 1972. The current situation in stress-corrosion studies. Metal Science Journal 6 (1), 238–240.

Scully, J., 1980. The interaction of strain-rate and repassivation rate in stress corrosion crack propagation. Corrosion Science 20 (8), 997–1016.

Shaikh, H., Amirthalingam, R., Anita, T., Sivaibharasi, N., Jaykumar, T., Manohar, P., Khatak, H., 2007. Evaluation of stress corrosion cracking phenomenon in an aisi type 316ln stainless steel using acoustic emission technique. Corrosion Science 49 (2), 740–765.

Smith, R., Cooper, J., 1989. A finite element model for the shape development of irregular planar cracks. International Journal of Pressure Vessels and Piping 36 (4), 315–326.

Sutton, M., Orteu, J., Schreier, H., 2009. Book-image correlation for shape, motion and deformation measurements, hardcover. Tech. rep., ISBN 978-0-387-78746-6.

Sutton, M., Wolters, W., Peters, W., Ranson, W., McNeill, S., 1983. Determination of displacements using an improved digital correlation method. Image and vision computing 1 (3), 133–139.

Takaya, S., Suzuki, T., Matsumoto, Y., Demachi, K., Uesaka, M., 2004. Estimation of stress corrosion cracking sensitivity of type 304 stainless steel by magnetic force microscope. Journal of nuclear materials 327 (1), 19–26.

Vermilya, D., Diegle, R., 1976. Concerning strain-enhanced corrosion mechanisms of scc. Corrosion 32 (1), 26–29.

Vermilyea, D., 1972. A theory for the propagation of stress corrosion cracks in metals. Journal of the Electrochemical Society 119 (4), 405–407.

Williford, R., Windisch, C., Jones, R., 2000. In situ observations of the early stages of localized corrosion in type 304 ss using the electrochemical atomic force microscope. Materials Science and Engineering: A 288 (1), 54–60.